LUCIANO COUTINHO CALDAS

IN-DUCT BEAMFORMING AND MODE DETECTION USING A CIRCULAR MICROPHONE ARRAY FOR THE CHARACTERISATION OF BROADBAND AEROENGINE FAN NOISE

São Paulo — Brazil

2016

LUCIANO COUTINHO CALDAS

IN-DUCT BEAMFORMING AND MODE DETECTION USING A CIRCULAR MICROPHONE ARRAY FOR THE CHARACTERISATION OF BROADBAND AEROENGINE FAN NOISE

Master dissertation submitted to Escola Politécnica at the University of São Paulo in partial fulfillment of the requirements for the degree of Master of Science

Concentration Area:
Electronic Systems

Advisor: Prof. Dr. Luiz Antonio Baccalá

São Paulo — Brazil

2016

LUCIANO COUTINHO CALDAS

IN-DUCT BEAMFORMING AND MODE DETECTION USING A CIRCULAR MICROPHONE ARRAY FOR THE CHARACTERISATION OF BROADBAND AEROENGINE FAN NOISE

Dissertação de mestrado apresentada à Escola Politécnica da Universidade de São Paulo para obtenção do título de Mestre em Ciências

Área de Concentração:
Sistemas Eletrônicos

Orientador: Prof. Dr. Luiz Antonio Baccalá

São Paulo — Brazil

2016

Este exemplar foi revisado e corrigido em relação à versão original, sob responsabilidade única do autor e com a anuência de seu orientador.

São Paulo, _____ de _____ de _____

Assinatura do autor: _____

Assinatura do orientador: _____

Catalogação-na-publicação

Caldas, Luciano Coutinho

In-duct beamforming and mode detection using a circular microphone array for the characterisation of broadband aeroengine fan noise / L. C. Caldas -- versão corr. -- São Paulo, 2016.

87 p.

Dissertação (Mestrado) - Escola Politécnica da Universidade de São Paulo. Departamento de Engenharia de Telecomunicações e Controle.

1.Beamforming 2.Processamento de sinais acústicos 3.Medições aeroacústicas 4.Ruído de fan 5.Análise modal I.Universidade de São Paulo. Escola Politécnica. Departamento de Engenharia de Telecomunicações e Controle II.t.

To my parents.

ACKNOWLEDGEMENTS

It is important to mention that this work was developed within the project *AERONAVE SILENCIOSA*, an EMBRAER/university partnership. Hence many people have been involved in one way or another. We should mostly like to thank those directly involved: Rudner L. Queiroz, Prof. Dr. Paulo C. Greco, Prof. Dr. Luiz A. Baccalá, Prof. Dr. Fernando M. Catalano, Prof. Rafael G. Cuenca, Bernardo Rocamora and Fernanda Nascimento.

To my advisor, Prof. Dr. Luiz A. Baccalá, who provided me all necessary support during this seemingly almost endless master study, I thanks for all cafés and useful discussions at the Poli-elétrica cafeteria and to the support during all my "down" moments during this journey.

To all friends, colleagues, technicians, engineers, professors and employees from the Aeronautical Engineering department of the USP-São Carlos and from the Telecommunications and Control Engineering Department at POLI-USP.

Special thanks go to Prof. Dr. Luiz A. Coelho and Prof. Dr. Guido Stolfi who helped me with many 'engineering tips' during the construction of the fan rig.

I also thank all friends from my home at São Carlos called "República nois que tah", similar to a "Fraternity", where we share all sorts of good and bad moments, mostly the former ones. Also, to friends from São Paulo, when I lived there during the first year as a part of this project.

To NASA Glenn Research Center staff, specially Daniel Sutliff, whose support and technical insight proved very helpful.

I'm very thankful to my parents who, despite living more than 1200 km away from my city, have been constantly in touch with me, supporting me during all ups and downs of this journey.

Finally, I would like to thank FINEP and Embraer for their financial support.

ABSTRACT

The development of technologies to reduce turbofan engine noise reveals the fan noise, the first stage of an engine, as a great contributor for the total noise of an airplane. So a better understanding of the fan noise generation came up and motivated the construction of a fan rig test facility at the University of São Paulo in São Carlos by a partnership between the university and EMBRAER S.A..

The fan rig is composed of a long duct (12 m long) comprising a 16-bladed fan rotor and 14-vaned stator. The rotor is powered by an 100 hp electrical motor allowing speed up to 4250 RPM resulting in 0.1 Mach axial flow. A 77-microphone wall-mounted array was designed for fan noise analysis. A cooperation with NASA-Glenn allowed data and information exchanging from their similar fan rig setup, the ANCF, grating then the validation of the in-house developed software. A short guide for duct-array is proposed in this work.

Complex software was developed to process the data from the microphones array. We performed 3 different types of analysis: power spectral density, noise imaging obtained by acoustic beamforming and modal analysis. We proposed a different technique for modal analysis based on beamforming images in this work. We did not find any similar technique in the references. The results obtained by this technique were validated with data from ANCF-NASA.

Comparative results are presented for both fan rigs, such as: power spectral densities for different fan speeds, modal analysis at the blade passing frequency (strong tones generated by the fan), noise imaging obtained by beamforming for rotating and static noise sources.

Finally, results achieved in this work are in agreement with those observed in the references consulted.

Keywords: Beamforming, Acoustic signal processing, Aeroacoustic measurement, Fan noise, Modal Analysis.

RESUMO

Com o desenvolver de tecnologias para redução de ruído de motores aeronáuticos turbofans, o ruído gerado pelo fan (primeiro estágio do motor) vem se mostrando cada vez mais um grande contribuinte na emissão total de ruído em um avião. Com isso, a necessidade de se estudar mecanismos geradores de ruído nestes motores veio à tona e motivou a construção de uma bancada de experimentos aero-acústicos junto à Universidade de São Paulo, campus São Carlos, oriundo da parceria entre EMBRAER S.A. e Universidade de São Paulo.

A bancada de ensaios compõe um conjunto rotor/estator, sendo que o fan (rotor) é equipado com 16 pás e a estatora 14 pás, conectado a um motor elétrico de 100 hp através de um eixo ao rotor, alcançando 4250 RPM com velocidade de escoamento axial médio de 0,1 Mach. Esta bancada é composta por um longo duto e a seção de ensaio com o fan localiza-se ao centro. Uma antena dispondo de 77 microfones foi especialmente projetada para fazer aquisição do ruído gerado pelo fan. Uma parceria com a *NASA-Glenn* possibilitou a troca de informações e dados experimentais de sua bancada de experimentos similar (*ANCF*) ajudando assim a validar os códigos desenvolvidos bem como comparar resultados para ambas as bancadas. Um pequeno roteiro para projeto de antena para análise modal e beamforming em duto é apresentado neste trabalho.

Um complexo *software* foi desenvolvido a fim de processar sistematicamente os dados aquisitados pelos microfones da antena. Três tipos de análise são feitas: Via espectro densidade de potência; Imagem de ruído acústico obtido através da técnica de *beamforming*, e por último, análise modal. Uma técnica diferente para análise modal baseada em imagens obtidas através de beamforming é proposta neste trabalho. Nada similar foi encontrado nas referências consultadas. Os resultados foram validados com dados de fontes sintéticas produzidas pela bancada *ANCF-NASA*.

Resultados comparativos para ambas as bancadas são exibidas neste trabalho, tais quais: Análise do espectro densidade de potência para diferentes rotações do fan; análise modal

nas frequências de passagem das pás (forte ruído tonal gerado pelo fan); imagem acústica do ruído gerado tanto por fontes rotativas quanto para fontes estáticas.

Finalmente, os resultados obtidos estão de acordo com o esperado e de antemão observados nas referências consultadas.

Palavras-chave: Beamforming, Processamento de sinais acústicos, Medições aeroacústicas, Ruído de fan, Análise modal.

LIST OF ABBREVIATIONS AND ACRONYMS

$NASA$	National Aeronautics and Space Administration
$ANCF$	Advanced Noise Control Fan
USP	University of São Paulo
DLR	German Aerospace Center
BPF	Blade passing frequency
PSF	Point spread function
CSM	Cross spectral matrix
BW	Beamwidth
DR	Dynamic Range
ICD	Inlet Control Device
VRM	Virtual Rotating Microphones
PSD	Power Spectral Density

LIST OF SYMBOLS

b	Conventional Beamforming map
N	Number of microphones
$\mathbf{g}$	Modal steering vector
$\mathbf{w}$	Normalized steering vector
$\mathbf{f}$	Vector of source strengths
$S_{x,y}$	Cross spectrum density between signals x and y
C	Cross spectral matrix
L	Data taper length
$J_m(x)$	First kind Bessel function of order m
$N_{m,n}$	Mode normalization
ψ	Mode shape function
a	Duct radius
Ω	Fan speed
M	Axial Mach number
M_t	Blade-tip Mach number
c	Sound speed
p	Acoustic pressure
$\mathbf{p}$	Vector of acoustic pressures
f	Frequency
f_s	Sampling frequency
k_0	Acoustic free wave vector
k_z	Axial wave number
$k_{m,n}$	Mode eigenvalue
$\mathbf{x} = r, \theta, z$	Vector in cylindrical coordinates
$\mathbf{x} = x, y, z$	Vector in rectangular coordinates
j	Complex number $\sqrt{-1}$
$E\{\cdot\}$	Expectation operator

$\mathscr{F}\{\cdot\}$	Discrete time Fourier transform
$\square^{+}$	Pseudo inverse operator
$\square^{H}$	Hermitian transpose operator

Subscript

i	Sensor point
s	Source mesh point
j	Source point for PSF computation
m, n	Circumferential and radial mode

CONTENTS

INTRODUCTION **13**

1 BACKGROUND THEORY **15**

1.1 Classical Beamforming **15**

1.2 Duct Beamforming **17**

1.2.1 Rotating frame 21

1.2.2 Limits of mode orders: m^- and m^+ 22

1.3 Point Spread Function - PSF **24**

1.4 Duct modes analysis **30**

2 SIGNAL PROCESSING TECHNIQUES **33**

2.1 Tone removal **33**

2.2 Virtual rotating microphones - VRM **36**

2.3 Data resampling **37**

2.4 Power spectral density (PSD) estimation **38**

2.4.1 PSD Estimation Details 39

3 EXPERIMENTAL SETUP **41**

3.1 University of São Paulo (USP) fan rig test facility **41**

3.1.1 Antenna design 42

3.1.2 Acoustic data acquisition system 46

3.1.3 Blade trip strip 47

3.2 Advanced Noise Control Fan - ANCF - NASA Glenn **47**

4 BEAMFORMING SOFTWARE **51**

4.1 Breakdown structure **51**

5 EXPERIMENTAL RESULTS **55**

5.1 Fan noise power spectral density 56
5.1.1 Raw power spectra 56
5.1.2 Removed Tones 58
5.1.3 Rotating spectra 59
5.2 Mode detection: Synthetic mode generator at ANCF-NASA Glenn . 61
5.3 Tyler-Sofrin modes 62
5.4 ANCF-NASA beamforming results 65
5.4.1 Static beamforming 65
5.4.2 Rotating beamforming 66
5.4.3 Mode detection: Array limitation 69
5.5 USP fan rig beamforming results 69
5.5.1 Static beamforming 70
5.5.2 Rotating beamforming: Gurney-flap 71
5.5.3 Rotating beamforming: Baseline 72

6 DISCUSSION AND CONCLUSIONS 75

BIBLIOGRAPHY 77

ANNEX 80

ANNEX A – MATLAB EXAMPLE CODES 81

INTRODUCTION

The present text dissertation results from a 3-year study in the Electrical Engineering - Signal Processing field, part of a project called *AERONAVE SILENCIOSA*, resulting from a partnership between University of São Paulo (São Carlos and Escola Politécnica Engineering Schools) and EMBRAER S.A.. The project aimed the construction of a fan rig test facility at USP - São Carlos for fan noise analysis and was financially supported by FINEP (Federal founding for development of science and research). The rig test facility was designed & assembled by technicians and engineers of USP with the cooperation of Embraer's engineering team. Moreover, the project was developed in collaboration with NASA-Glenn Research Center.

The aim of the project is just same as introduced in (1): "In modern high-bypass-ratio turbofan engines fan noise is a critical component controlling the total noise at takeoff and approach conditions. A better understanding of the fan noise generation, propagation, and radiation will aid in the design of noise suppression devices to alleviate community noise problems. A typical fan noise spectrum consists of tone noise [blade passing frequency (BPF) and its harmonics] superimposed over broadband noise. The fan tone noise is the result of interactions of periodic disturbances of the rotor-blade mean wakes with the stator vanes. This is usually referred to as rotor-stator interaction noise, and it is the component considered here."

The goal of this study was to develop a reliable tool for fan noise broadband analysis in terms of its power spectral density (PSD), beamforming imaging and mode detection by the use of acoustic pressure data acquired from an array of microphones specially designed for that purpose.

Unfortunately, beamforming imaging is still a recent technique and there are not a great number of references available. This is even worse for rotating and duct beamforming. The guidelines provided by Lowis in (2) reveals many details about the sound propagation within a duct and rotating beamforming techniques. Dougherty in (3–5) shows a great number of experimental results and suggestions to modify slightly the formulation discussed

by Lowis. Sitjsma in (6) and Sutliff in (7) with techniques for mode detection using a rake of microphones inside the duct. All these references were used in order to achieve our purpose: the characterization of broadband aeroengine fan noise.

In addition to the referred work, this study proposes a guideline to project duct-array of microphones for fan broadband noise. Furthermore, a technique for modal analysis based on beamforming imaging is also proposed.

The analysis performed in this study uses experimental data from two fan rig test facilities: ANCF-NASA Glenn and USP fan rig. Convenient results are compared with each other.

For the sake of cohesion and coherence the text is divided into chapters as follows:

Background theory - All the necessary background theory is exposed in order to understand how we obtained the results reported here.

Signal processing techniques - As the beamforming process requires a great number of signal processing, this chapter expose the techniques necessary to perform the duct-beamforming for fan noise analysis.

Experimental setup - Details from both fan rig test facilities (USP and ANCF) are provided, such as: geometry, performance parameters, schematics, microphone array, etc.

Beamforming software - The signal path flow are block diagrammed to summarize how the software performs the beamforming imaging, mode detection and the power spectral density (PSD).

Experimental results - A great number of experimental results obtained for both rigs are presented.

Finally: *Discussion and Conclusions, Bibliography* and *Annex*.

1 BACKGROUND THEORY

When sound propagates within ducts, its behaviour can be described as a sum of "modes" where each mode is an eigensolution of the wave equation that couples with duct boundary conditions. To perform modal decomposition one can estimate the amplitude of each modal component from pressure signal measurements via duct-wall mounted microphones.

The following sections present the relevant concepts together with the state-of-the-art beamforming techniques and their application to the problem.

1.1 CLASSICAL BEAMFORMING

Beamforming is a technique that attempts to solve the "inversion problem", i.e., whereby the observation of the magnitude of a physical quantity at a point, say pressure in our case, allows the inference of that signal/information at a distance from reaching that point. This requires knowing the traveled path.

Pressure signals measured at several known positions are used to move them backward in time to a desired point in space. This requires knowing how sound waves propagate under those circumstances. In the duct propagation case, the sound wave propagation equation must be supplemented with adequate boundary conditions.

To probe the sound producing environment, it is common to define a suitable mesh of desired points, i.e., a finite number of discrete virtual candidate sources, forming an acoustic pressure density distribution map over the mesh surface.

If we introduce the dipole source distribution specified by $\mathbf{f}(\vec{x}_s) = \mathbf{f}(x_s, y_s, z_s)$ (the subscript 's' denotes the source position) one needs to determine an adequate transfer impedance matrix $\mathbf{G}$ that maps how the sound from mesh points translates into observations. This is usually done as follows:

$$\mathbf{p} = \mathbf{G}\mathbf{f} \tag{1.1}$$

where **p** is the vector of pressure measurements at the array of microphones due to the mesh discretized sound sources, **in the frequency domain**. The matrix **G** relates source strength distribution **f** to the sound pressure vector **p**. In other words, **G** describes how the wave propagates from the desired source point to the microphone positions. The $(i, j)^{th}$ element of **G** specifies the transfer impedance between the i^{th} source in the mesh and the pressure at the j^{th} microphone.

Undesired noise in the pressure signals **p** is usually modeled as additive error **e**:

$$\hat{\mathbf{p}} = \mathbf{G}\mathbf{f} + \mathbf{e}. \tag{1.2}$$

The optimal minimum mean square error source strength vector **f** is given by

$$\mathbf{f} = \mathbf{G}^{+}\hat{\mathbf{p}} \tag{1.3}$$

where $\mathbf{G}^{+} = [\mathbf{G}^{\mathbf{H}}\mathbf{G}]^{-1}\mathbf{G}^{\mathbf{H}}$ is the pseudo-inverse of **G** and ^{H} denotes the Hermitian transpose operator. Use of (1.3) guarantees that $\mathbf{e}^{\mathbf{H}}\mathbf{e}$ is minimum.

Now consider the cross-spectral matrix (CSM) of the measured pressures $C_{\hat{p}\hat{p}}(\omega)$ given by

$$C_{\hat{p}\hat{p}} = \frac{\pi}{T} E\{\hat{\mathbf{p}}\hat{\mathbf{p}}^{H}\} \tag{1.4}$$

$E\{\cdot\}$ detones the expectation value. Substituting Eq. 1.1 into 1.4 leads to

$$C_{\hat{p}\hat{p}} = \mathbf{G} B_{ff} \mathbf{G}^{\mathbf{H}} \tag{1.5}$$

where

$$B_{ff} = \frac{\pi}{T} E\{\mathbf{f}\mathbf{f}^{\mathbf{H}}\} \tag{1.6}$$

Equivalently, to determine B_{ff} from $C_{\hat{p}\hat{p}}$, Eq. 1.3 is substituted into 1.6 so that

$$B_{ff} = \mathbf{G}^{+} C_{\hat{p}\hat{p}} (\mathbf{G}^{+})^{H} \tag{1.7}$$

Eq. 1.7 is finally the well known equation for the conventional beamforming method. The cross-spectral matrix $C_{\hat{p}\hat{p}}$ is estimated for all pressure-signals from microphones in the

array. The steering vector $\mathbf{G}^+$ is evaluated at all mesh-points to the microphones locations. The steering vector formulation must consider all the paths linking the mesh points to the corresponding microphone.

For this, it is necessary to introduce the convected wave equation

$$\Big(\nabla^2 - \frac{1}{c^2}\frac{D^2}{D\,t^2}\Big)p(t,\vec{x}) = 0 \tag{1.8}$$

where $D/D\,t = \partial/\partial\,t + c\,M(\partial/\partial\,z)$ is the derivative operator associated with a mean flow velocity of $c\,M$ in the z direction (axial direction for a duct), c is the sound speed in a uniform flow and M the Mach number. In the rectangular coordinates, $\vec{x} := (x, y, z)$, and in cylindrical coordinates, $\vec{r} := (r, \theta, z)$.

As an example to simplify the problem, let $M = 0$ and the boundary conditions be the free-field propagation. Then, the solution for Eq. 1.8 is

$$p(t,\vec{x}) = \frac{A}{4\pi|\vec{x}|}e^{j(\omega t - \vec{k}.\vec{x})} \tag{1.9}$$

where $\vec{k}$ is the wave number at a certain frequency and A a constant. In the free-field case, the steering vector is similar to Eq. 1.9. Sarradj has shown in (8) four different formulations for free-field steering vectors with different performance. For example one candidate would be

$$g(\vec{x}_i, \vec{x}_s, \omega) = \frac{1}{N}e^{-j\vec{k}.(\vec{x}_i - \vec{x}_s)} \tag{1.10}$$

As the free-field case is not the aim of this work, we do not examine this case any further. The following sections describe the solution for 1.8 with the hard-wall duct boundary conditions.

1.2 DUCT BEAMFORMING

To understand sound propagation within a duct and to formulate a steering vector for duct beamforming imaging, we use the formalism proposed in (4), (9), (10), (2) and (11).

Duct beamforming relies on the solution for the Eq. 1.8 with duct boundaries conditions defined by Eq. 1.13. In cylindrical coordinates, the operator ∇ becomes

$$\nabla^2 = \frac{\partial^2}{\partial z^2} + \frac{\partial^2}{\partial r^2} + \frac{1}{r}\frac{\partial}{\partial r} + \frac{1}{r^2}\frac{\partial^2}{\partial \theta^2}$$

and Eq. 1.8 becomes

$$\Big(\frac{\partial^2}{\partial r^2} + \frac{1}{r}\frac{\partial}{\partial r} + \frac{1}{r^2}\frac{\partial^2}{\partial \theta^2} + \big(1-M^2\big)\frac{\partial^2}{\partial z^2} - \frac{2M}{c}\frac{\partial^2}{\partial t\,\partial z} - \frac{1}{c^2}\frac{\partial^2}{\partial t^2}\Big)p(t,\vec{r}) = 0 \tag{1.11}$$

In the frequency domain, Eq. 1.11 is given by

$$\Big(\frac{\partial^2}{\partial r^2} + \frac{1}{r}\frac{\partial}{\partial r} + \frac{1}{r^2}\frac{\partial^2}{\partial \theta^2} + \big(1-M^2\big)\frac{\partial^2}{\partial z^2} - 2jMk_0\frac{\partial}{\partial z} + k_0^2\Big)p(\omega,\vec{r}) = 0 \tag{1.12}$$

where $\mathscr{F}\{\partial/\partial t\} = j\omega$ and $k_0 = \omega/c$ is the acoustic free wave number. The solution for a hard-wall duct boundary condition:

$$\left.\frac{\partial p}{\partial r}\right|_{r=a} = 0 \tag{1.13}$$

is expressed as a linear superposition of the modes inside the circular duct as

$$p(\omega,\vec{r}) = \sum_{m=-\infty}^{\infty}\sum_{n=0}^{\infty} A^+_{m,n}\Phi^+_{m,n}(r,\theta)e^{-jk_z^+ z} + \sum_{m=-\infty}^{\infty}\sum_{n=0}^{\infty} A^-_{m,n}\Phi^-_{m,n}(r,\theta)e^{-jk_z^- z} \tag{1.14}$$

where superscripts $^+$ and $^-$ indicate variables associated to positive and negative z-direction propagation, according to the coordinates system in Fig. 1. For the circular duct geometry, the acoustic modes are found in terms of spinning exponential functions in the circumferential direction. Bessel functions of the first kind $J_m(x)$ in the radial direction are then used.

$$\Phi_{m,n}(\vec{r}) = \frac{J_m(k_{m,n}r)}{N_{m,n}}e^{jm\theta}, \quad m = 0,\pm1,\pm2,\ldots \quad n = 0,1,2,\ldots \tag{1.15}$$

where $N_{m,n}$ is the modal amplitude and the argument $k_{m,n}$ is the mode eigenvalue. The solution in Eq. 1.15 is completely defined by finding the correct eigenvalue $k_{m,n}$ from the characteristic equation that represents the hard wall boundary condition, as in Eq. 1.13.

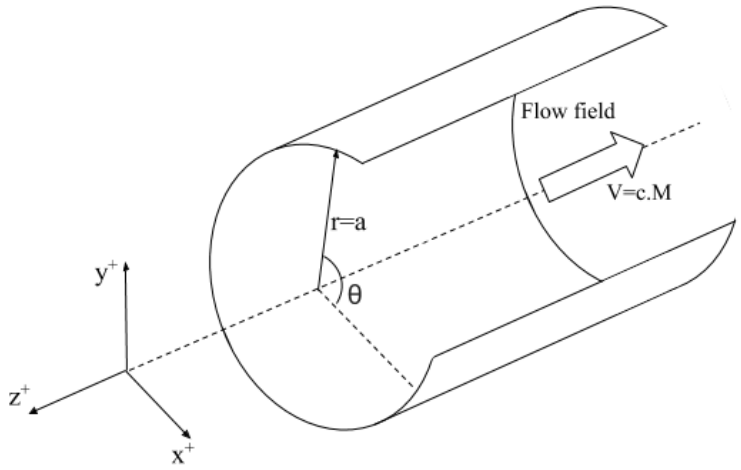

Figure 1 – Coordinates system used.

In addition, the axial wave numbers k_z are also associated with every mode and are found, from the following quadratic dispersion relationship, to be:

$$k_{m,n}^2 = k_0^2 - k_z^2(1-M^2) - 2k_0 k_z M \tag{1.16}$$

Solving Eq. 1.16 for k_z we have

$$k_z^{\pm} = \frac{-k_0 M \mp \sqrt{k_0^2 - (1-M^2)k_{m,n}^2}}{1-M^2} \tag{1.17}$$

Values of $k_{m,n}$ are computed in a way that $J'_m(k_{m,n}a) = 0$, i.e., the product $k_{m,n}a$ is the n^{th} stationary point of order m of the Bessel function $J_m(x)$. A table of these stationary values is reported in Ref (12). So, for each stationary value $k_{m,n}a$ corresponding to a combination of modes (m,n) we have an axial wave number $k_z^{\pm}$ associated.

A mode is called a *cut-on* mode when

$$k_0^2 - (1-M^2)k_{m,n}^2 > 0$$

i.e.,

$$k_{m,n} < \frac{k_0}{\sqrt{1-M^2}} \tag{1.18}$$

otherwise it is a cut-off mode which decays exponentially along the z-direction.

To define a source-receiver model, the steering vector $g(\vec{r}_i, \vec{r}_s, \omega)$, it is useful to define a function $\varphi(\vec{r})$, based on Eq. 1.14 and 1.15 such as

$$\varphi(\vec{r}) = \frac{J_m(k_{m,n} r)}{N_{m,n}} e^{jm\theta} e^{-jk_z^- z} \tag{1.19}$$

Let $f(\vec{r}_s, \omega)$ represent the pressure source so that the pressure $p(\vec{r}_i, \omega)$ at the microphone position $\vec{r}_i$ is

$$p(\vec{r}_i, \omega) = \int_{\mathbf{S}} f(\vec{r}_s, \omega) g(\vec{r}_i, \vec{r}_s, \omega) d\mathbf{S} \tag{1.20}$$

where **S** is the duct-section for sources located at the fan plate.

Lowis in (2) suggests at his Eqs. (2.2) and (2.3) that a good candidate for $g(\vec{r}_i, \vec{r}_s, \omega)$ is the Green's function:

$$g(\vec{r}_i, \vec{r}_s, \omega) = \frac{j}{4\pi} \sum_{m,n} \frac{\varphi^*(\vec{r}_s)\varphi(\vec{r}_i)}{\sqrt{k_0^2 - (1-M^2)k_{m,n}^2}} \tag{1.21}$$

However, Dougherty *et al.* have shown (4) an important implication of this choice for modes close to cut-off . Because the denominator of Eq. 1.21 tends to zero, the Green's function is dominated by these modes due to numerical errors and leads to unrealistic results of the beamforming based on this steering vector.

As mentioned before the steering vector definition is not unique. For the free-field case, Sarradj has shown (8) different formulations and their different characteristics. The situation is not different for the duct case. Modifications can be made in order to achieve more accurate and physically realistic descriptions.

In this way, the steering vector used here is the same one suggested by Dougherty *et al.* (4)

$$g(\vec{r}_i, \vec{r}_s, \omega) = \sum_{m,n} \varphi^*(\vec{r}_s)\varphi(\vec{r}_i) \tag{1.22}$$

Substituting Eq. 1.19 into 1.22 we obtain

$$g(\vec{r}_i, \vec{r}_s, \omega) = \sum_{m=-m^-}^{m^+} \sum_{n=0}^{n=n^+} \frac{J_m(k_{m,n} r_i) J_m(k_{m,n} r_s)}{N_{m,n}^2} e^{jm(\theta_i - \theta_s)} e^{-jk_z^-(z_i - z_s)} \tag{1.23}$$

The terms $m^- \leq m \leq m^+$ and $0 \leq n \leq n^+$ are determined according to Eq. 1.18,i.e., in the range of cut-on modes. The term $N_{m,n}^2$ is a mode normalization that should satisfy the energy conservation over the surface **S**

$$S^{-1} \int_{\mathbf{S}} |\varphi(\vec{r})|^2 d\mathbf{S} = 1 \tag{1.24}$$

Solving we have

$$N_{m,n}^2 = \frac{2}{a} \int_0^a |J_m(k_{m,n} r)|^2 r \, dr$$

$$N_{m,n}^2 = \Big(1 - \frac{m^2}{(k_{m,n} a)^2}\Big) |J_m(k_{m,n} a)|^2 \tag{1.25}$$

1.2.1 Rotating frame

The formulation of Section 1.1 covers strictly stationary sources within a hard-wall duct. If applied to rotating sources, for example, the rotor noise, the result will be rings of smeared noise, since the fan motion blurs the noise along the circumferential direction. In order to compensate this motion, some kind of synchronic mechanism must be applied to the technique. In terms of steering vector, this is made by changing the coordinates system, as described next. In Chapter 2 we argue that the microphone signals must be also compensated for the rotating sources.

Aiming to adapt the coordinate system for the rotating frame reference, for a spinning source with angular frequency Ω, the coordinate component radius r and z do not change. The only change is in the θ component

$$\theta' = \theta - \Omega t \tag{1.26}$$

Substituting Eq. 1.26 into 1.11 produces

$$\Big(\frac{\partial^2}{\partial r^2} + \frac{1}{r}\frac{\partial}{\partial r} + \frac{1}{r^2}\frac{\partial^2}{\partial \theta^2} + \big(1-M^2\big)\frac{\partial^2}{\partial z^2} + \frac{2M}{c}\Big(\Omega \frac{\partial^2}{\partial z \partial \theta'} - \frac{\partial^2}{\partial t \partial z}\Big) - \frac{1}{c^2}\Big(\frac{\partial^2}{\partial t^2} - 2\Omega \frac{\partial^2}{\partial \theta' \partial t} + \Omega^2 \frac{\partial^2}{\partial \theta'^2}\Big)\Big) p(t, \vec{r}) = 0 \tag{1.27}$$

which becomes

$$\Big(\frac{\partial^2}{\partial r^2}+\frac{1}{r}\frac{\partial}{\partial r}+\frac{1}{r^2}\frac{\partial^2}{\partial \theta^2}+\big(1-M^2\big)\frac{\partial^2}{\partial z^2}+\frac{2M}{c}\Big(\Omega\frac{\partial^2}{\partial z\partial \theta'}-j\omega\frac{\partial}{\partial z}\Big)-\frac{1}{c^2}\Big(-\omega^2-2j\omega\Omega\frac{\partial}{\partial \theta'}+\Omega^2\frac{\partial^2}{\partial \theta'^2}\Big)\Big)p(\omega,\vec{r})=0 \tag{1.28}$$

in frequency domain.

The solution for the Eq. 1.28 leads to the same Bessel equation as in Eq. 1.14 and 1.15 except for the wave number k_0, which is replaced by

$$k_0'=k_0-\frac{m'\Omega}{c} \tag{1.29}$$

where m' is the circumferential mode order in the rotating frame reference. Furthermore, Eq. 1.16 and 1.17 become

$$k_{m,n}^2={k'}_0^2-k_z^2(1-M^2)-2{k'}_0k_zM \tag{1.30a}$$

$$k_z^{\pm}=\frac{-{k'}_0M\pm\sqrt{{k'}_0^2-(1-M^2)k_{m,n}^2}}{1-M^2} \tag{1.30b}$$

Eq. 1.29 can be seen as a shift-frequency in the rotating frame. Another way to see that is

$$\omega'=\omega-m'\Omega \tag{1.31}$$

which is exactly the frequency shift that modes apply due to the shaft spinning speed.

The steering vector formulation remains unchanged as in Eq. 1.23 but with a corrected wave number (Eq. 1.30b) due to the rotation effects.

1.2.2 Limits of mode orders: m^- and m^+

After introducing the rotating frame reference and the rotating steering vector, it is important to mention some differences in the range of cut-on modes in Eq. 1.23 compared to those expected for the static and rotating modes.

By the Eq. 1.18 the range of cut-on modes in the stationary frame can be easily determined. However, in terms of rotating frame, changes on k_0' by Eq. 1.30b promote slightly variations on the estimated range.

If we substitute Eq. 1.29 into 1.30b and take the positive values within the square root in order to estimate the new range of cut-on spinning modes, we have

$$k_{m,n} < \frac{k_0 \pm mM_t}{\sqrt{1-M^2}} \tag{1.32}$$

where $M_t = \Omega a/c$ is the blade Mach tip.

If at least one radial mode of order m can propagate at a frequency $\omega - m\Omega$, that gives $|\omega - m\Omega| > \omega_{m,0}$, where $\omega_{m,0}$ is the cut-off frequency of the lowest order radial mode $n = 0$. This can be rewritten as

$$|ka \pm mM_t| \geq (ka)_{m,0} \tag{1.33}$$

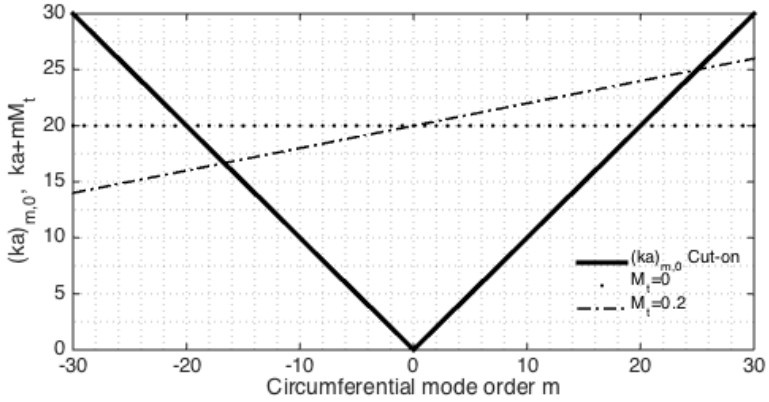

Figure 2 – Circumferential modes. Cut-on frequencies $(ka)_{m,0}$ in bold line. Two different lines (dotted in dashed) for the cut-on condition $ka + mM_t$ versus mode order m. (ka) is fixed in 20 and two different tip Mach is shown. Curves intersection define $m^{\pm}$.

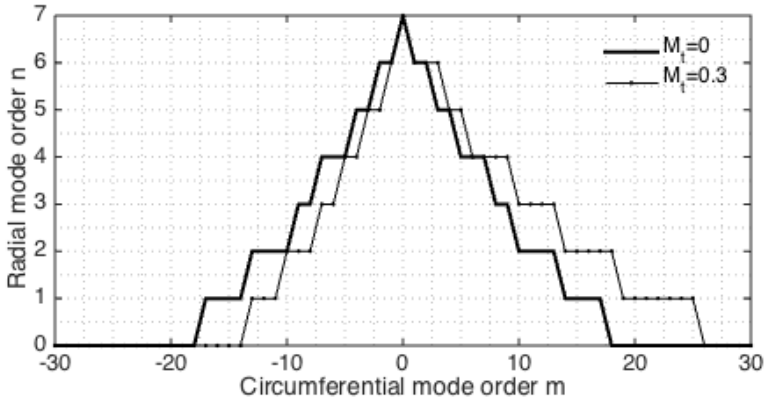

Figure 3 – The cut-on spinning modes shape for two different tip Mach conditions. The effect of the fan spinning in the generation of asymmetric modes order.

This equation gives the range of cut-on spinning modes depending on the Mach tip. Fig. 2 shows in bold line, the cut-on frequency $(ka)_{m,0}$ corresponding to the right hand

side of Eq. 1.33. The dashed and dotted lines corresponds to different Mach tip situations, one for $M_t = 0$ and other for $M_t = 0.2$. The range of cut-on modes is described by the range between both intersections of the curve $(ka)_{m,0}$ and the corresponding M_t.

For example, for $M_t = 0$ we have $m = \pm 20$, same range for positive and negative. However, for $M_t = 0.2$, we have approximately $m^- = -17$ and $m^+ = +25$. This result can also be seen in Fig. 3, where the Eq. 1.32 is plotted for two different Mach tips. It is important to mention that positive spinning modes (m^+) are also called co-rotating modes, i.e., which spins in the same direction of the rotor. On the other hand, negative spinning modes (m^-) spins in counter-rotating direction with reference to the rotor.

Another way to estimate the range of modes $m^\pm$ is by means of the angular phase velocity c_p of the mode m at the duct wall, which is given by $c_p = a\omega/m$ and must exceed the sound speed c in order to propagate. This calculation does not consider the axial flow. So, in the rotating reference frame, the cut-off condition becomes $c_p - a\Omega > c$.

Substituting Eq. 1.32 into 1.33 we have

$$\frac{ka}{m} - M_t \geq 1$$

$$m^\pm = \frac{ka}{1 \mp M_t} \tag{1.34}$$

which is in agreement with Fig. 2. Finally, Eq. 1.34 reveals that for $M_t \to 1$, $m^+ \to \infty$, as also predicted in Fig. 2 and 3.

1.3 POINT SPREAD FUNCTION - PSF

We can introduce a generic definition for the PSF as follows: The point spread function (PSF) describes the imaging system response to a point input, and is analogous to the impulse response. A point input, represented as a single pixel in the “ideal” image, will be reproduced as something other than a single pixel in the “real” image. This final image obtained, in the context of acoustic imaging by an array of microphones, is the response of that array due to a source point in the space.

For a certain point in space ξ_s at some frequency f, a point source can be placed and the beamforming map is then built due to this source. Ideally, a very small spot would be visualized in the map at the source location. However, due to limitation of the array (concerning size and number of sensors) the latter statement no longer holds. The spot is not small enough and there are side-lobes in the image. As an example, Fig. 6 shows the PSF of an array with 62 sensors just as in Fig. 4. The frequency is 8 kHz and the source is placed 1 m from the array.

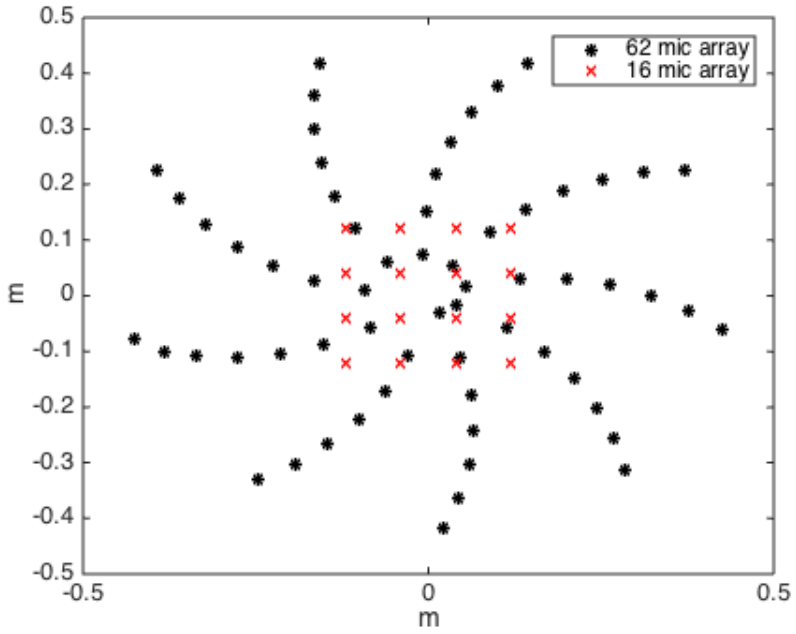

Figure 4 – Two different arrays geometry. 62-microphones in log-spiral configuration (black dots) and Rectangular 16-mics configuration (red crosses).

To understand why, one could make a mathematical analogy with linear systems, suppose a linear system with transfer function such as:

$$H(f) = 1$$

in a way that impulse outputs remain equal to their inputs. In other words, an ideal array would have a PSF equivalent to this transfer function, so that the final image due to a source point would be exact only this source point, i.e., the system's output remains the same as the input. For more details about linear systems (13–15). Nonetheless, consider a transfer function $H(f)$ for an ideal low-pass filter (also called as sinc filter) instead of an unit gain, limiting then the bandwidth. Its transfer function is then given by

$$H(f) = rect(\frac{f}{2B})$$

where B is an arbitrary cutoff frequency (or bandwidth).

If an impulse $\delta(t)$ is applied to it, the output is

$$h(t) = \mathscr{F}^{-1}\{H(f)\} = 2B\frac{sin(2\pi Bt)}{2\pi Bt} = 2Bsinc(2Bt).$$

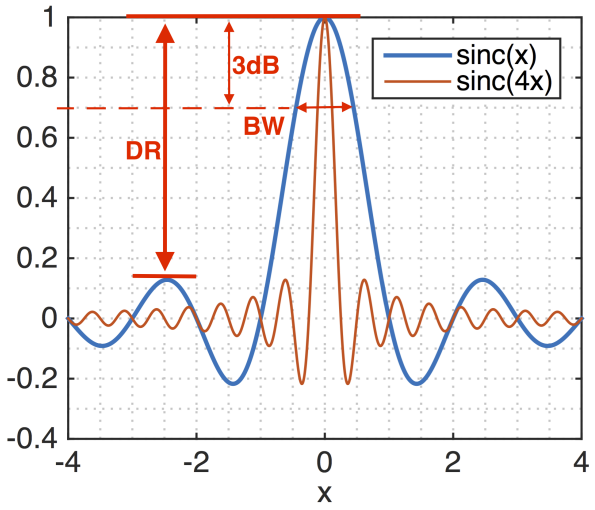

Figure 5 – Two different plots for the $sinc(.)$ function that can be further associated with a PSF map. Beamwidth (BW) and dynamic range (DR) are indicated for performance measurements.

Fig. 5 shows a typical plot for a sinc response. The PSF map has a form similar to a sinc function, even though it is three-dimensional, as in Fig. 6. The bandwidth limitation (above cited) can then be seen as array limitation specifically the finite aperture (spatial extent) of the limited number of microphones.

For example, the two functions $sinc(x)$ and $sinc(4x)$ in Fig. 5 would represent the PSF response of two different arrays. The one with more sensors and bigger aperture would have its PSF represented by $sinc(4x)$ corresponding to a narrow beamwidth and lower side lobes level. By contrast, smaller configurations with fewer sensors would be represented by $sinc(x)$.

Thus, the point-spread function is commonly used to see how a point source reveals itself within the array. This is commonly used to measure the array's performance in terms of beamwidth (BW) and sidelobe levels (or dynamic range - DR) in Fig. 5. A narrow beam and lower side lobe levels define better array performance.

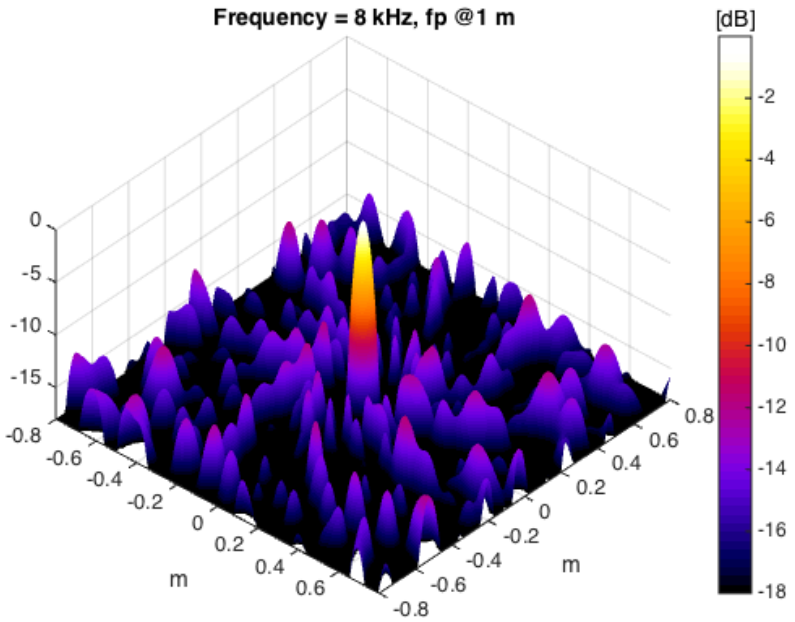

Figure 6 – PSF for the 62-mic antenna shown in Fig. 4 at 8 kHz and 1 m away revealing the similarity with the sync functions depicted in Fig. 5.

To represent the PSF map, a point source can be modeled in terms of radiation directivity, as a monopole or a dipole. In this particualr study, point sources are going to be treated as dipoles, as done by Lowis (2) and Sitjsma (16). The effect of a dipole stationary tonal source, denoted $\vec{j}$, was simulated following the guidelines provided by Sijtsma (16). This source induces a CSM given by

$$C_j = \vec{g}_j^H \vec{g}_j = \vec{w}_j^H \vec{w}_j \tag{1.35}$$

where $\vec{w}$ is the steering vector for unit power source. The beamforming map is obtained by scanning the grid points ξ_s leading to

$$b_{js} = \vec{w}_s C_j \vec{w}_s^H = \vec{w}_s (\vec{w}_j^H \vec{w}_j) \vec{w}_s^H = ||\vec{w}_s \vec{w}_j^H||^2 \tag{1.36}$$

which means that the PSF map can be obtained by fixing the steering vector $\vec{w}_j$ at the source position while sweeping $\vec{w}_s$ over the image mesh grid ξ_s. As an example, Fig. 7 shows a 16-mic array (blue circles) and an arbitrary mesh located 1 m away (black dots). The sweeping is made over this fixed mesh.

For the free-field case and the arrays in Fig. 4, the PSF maps are presented in Fig. 8. As the frequency increases, the beam becomes more narrow. The fewer sensors array,

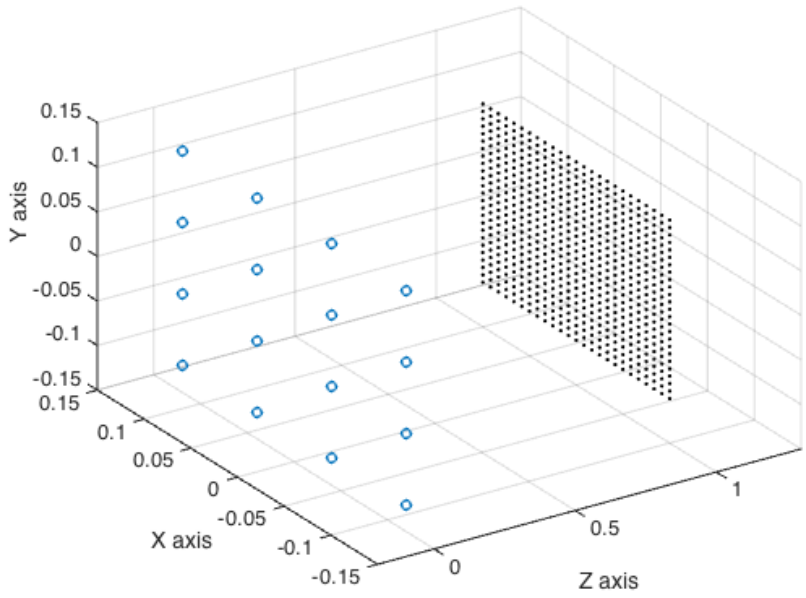

Figure 7 – 16-mic array (blue circles) and an arbitrary 25 by 25 points mesh (black dots).

16-mic, has a much wider beam (top plots) in comparison to the 62-mic (bottom plots). Besides, it is possible to see an aliasing process happening for the top-right plot, i.e., the repetition of the main lobe periodically in the space. This *phenomena* is similar to the Nyquist *criteria* (14) and because of the array limitation, there is a limited region in the space that the beamforming can sweep. Outside of this region, a periodic repetition of the main lobe appears and consequently leads to noise sources that appear in the map where in fact no source is physically present.

The formulation presented above is independent of the steering vector formulation. We already introduced PSF maps for the free-field case (Fig. 8). Regarding the Eq. 1.23 for the modal steering vector, the duct PSF can also be performed in order to visualize its effects within the duct.

For the USP fan rig geometry, a simulation example can be applied in Fig. 9 for a source located at $r = 0.15\ m$, $\theta = 0$ and $z = -0.71\ m$. This focal plane (fp), the z distance, is the same of the fan plane. Frequencies in the range between the 1st and 4th BPF equivalent for 4250 RPM were evaluated. The USP array and rig geometry are detailed in Chapter 3.

It is important to mention that, due to the small number of modes at low frequencies, the source location on the PSF map does not match exactly the desired point $\vec{j}$, and the map

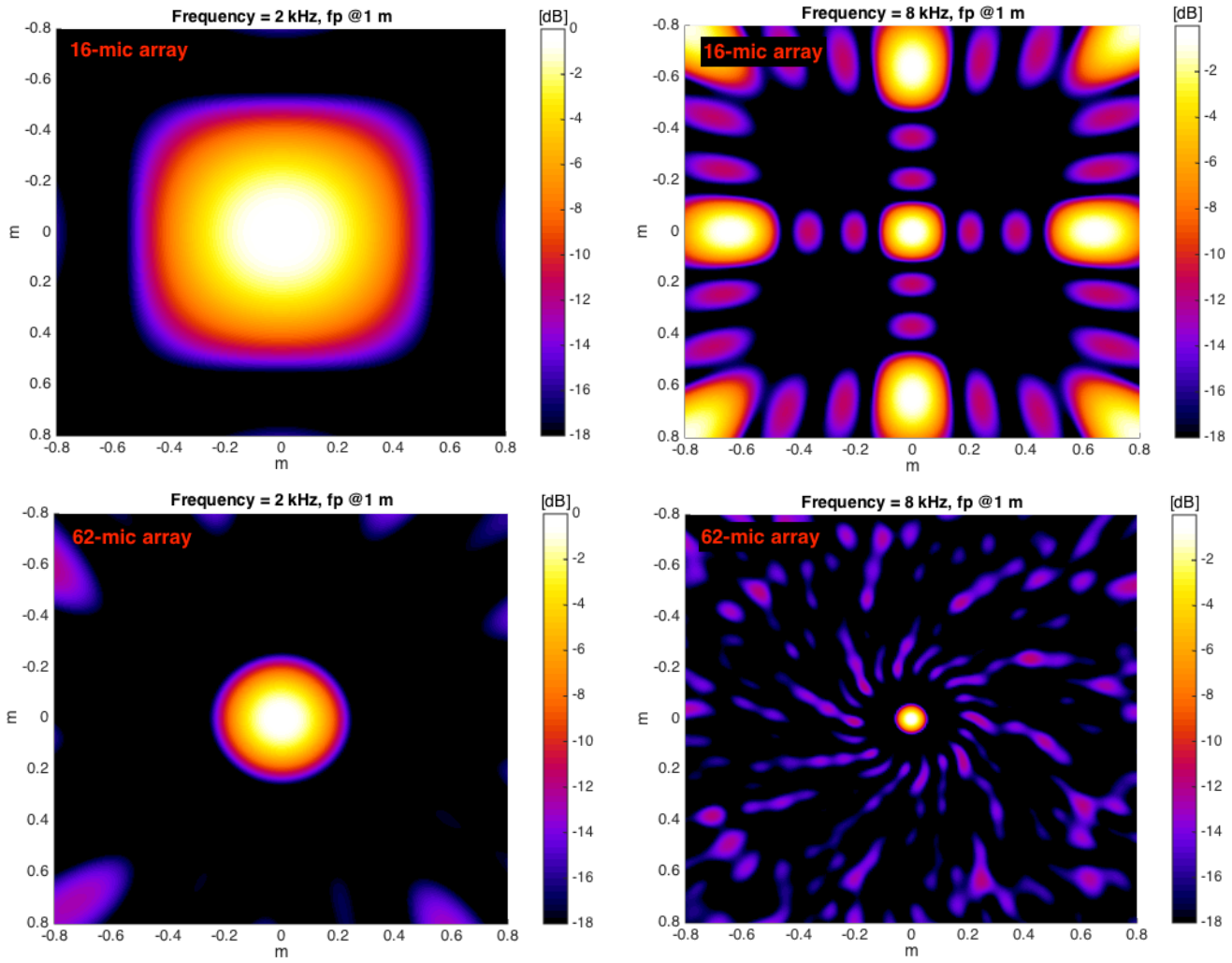

Figure 8 – PSF for the arrays on Fig. 4 at two frequencies: 2 and 8 kHz. Source 1 m away. Top maps regard the 16-mic array and bottom maps, the 62-mic array.

has a large main lobe. At 1.13 kHz a clearly discernible source close to the wall is observed and comprises only 11 cut-on modes. Strong beamforming side-lobes can also be seen. At higher frequencies source discernibility increases followed by diminished side-lobes confirming code plausibility.

For the ANCF rig at NASA, results for PSF can also be applied. The NASA array (detailed also in Chapter 3) has many more microphones (around 90) as compared to the USP fan rig's 77 mics. As already discussed, better performance is expected for this array relative to USP's fan rig array.

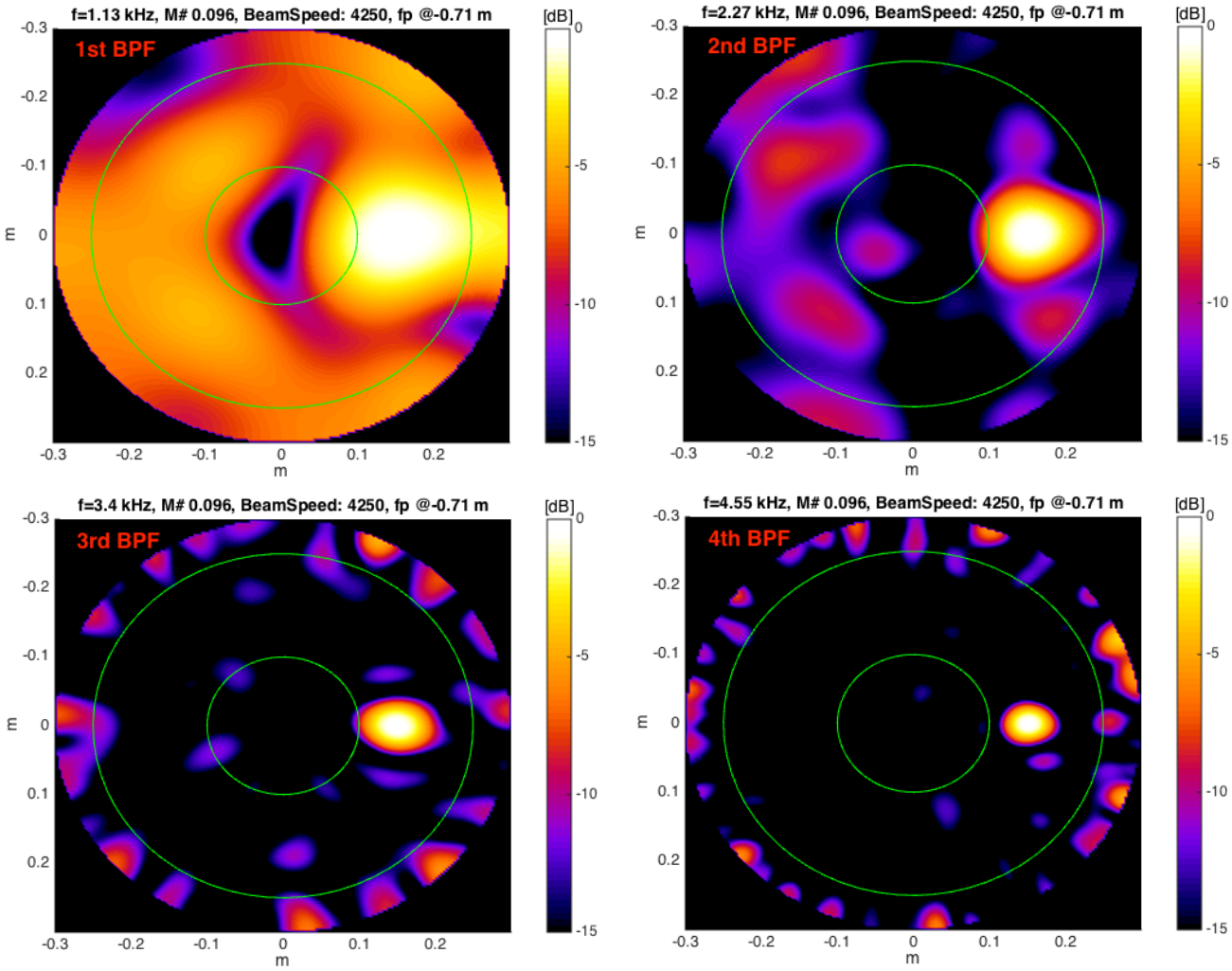

Figure 9 – PSF for the duct steering vector formulation. USP fan rig configuration for duct-radius and focal plane distance. Frequencies are evaluated from the 1^{st} to the 4^{th} BPF equivalent for a 4250 RPM shaft speed.

1.4 DUCT MODES ANALYSIS

Unfortunately no references for modal analysis were found in the literature. Dougherty shows good results for modal analysis in (3) and (5) but it is unclear how to perform them.

Close inspection of equations 1.21 and 1.23 reveals that g_i can be re-written in a double sum involving circumferential and radial modes (m,n)

$$g = \sum_m \sum_n g_{m,n} \tag{1.37}$$

(the subscript i was suppressed to simplify notation). Thus beamforming results can be

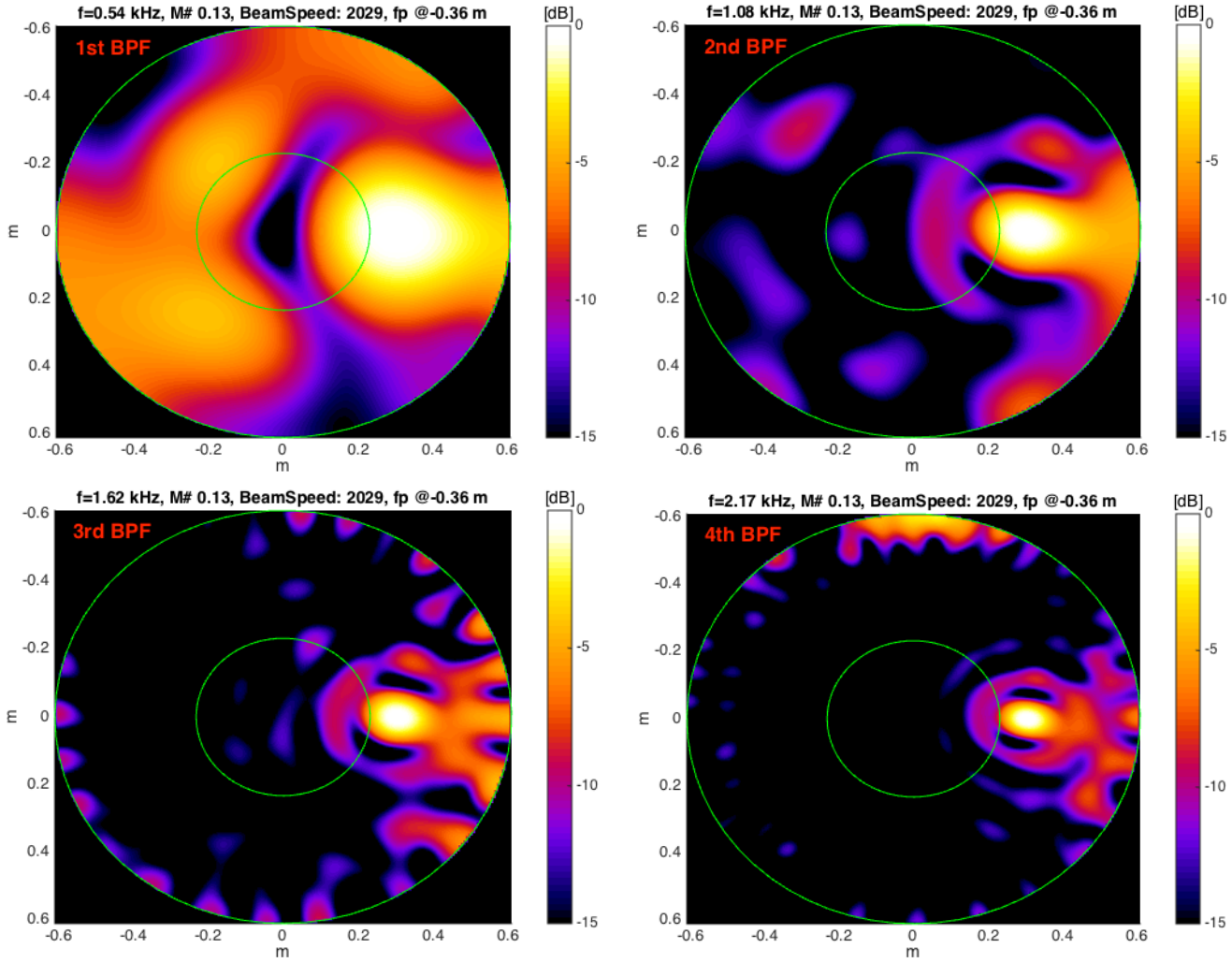

Figure 10 – PSF for the duct steering vector formulation. ANCF-NASA fan rig configuration for duct-radius and focal plane distance. Frequencies are evaluated from the 1^{st} to the 4^{th} BPF equivalent for a 2029 RPM shaft speed.

broken into modes:

$$\mathbf{B_{modes}} = \begin{bmatrix} \mathbf{g_{1,0}} \\ \mathbf{g_{1,1}} \\ \vdots \\ \mathbf{g_{m,n}} \end{bmatrix} C\left[\mathbf{g_{1,0}^H}\ \mathbf{g_{1,1}^H} \cdots \mathbf{g_{m,n}^H}\right] = \begin{bmatrix} \mathbf{g_{1,0}} C\mathbf{g_{1,0}^H} & \mathbf{g_{1,0}} C\mathbf{g_{1,1}^H} & \cdots & \mathbf{g_{1,0}} C\mathbf{g_{m,n}^H} \\ \mathbf{g_{1,1}} C\mathbf{g_{1,0}^H} & \mathbf{g_{1,1}} C\mathbf{g_{1,1}^H} & \cdots & \mathbf{g_{1,1}} C\mathbf{g_{m,n}^H} \\ \vdots & \vdots & \ddots & \vdots \\ \mathbf{g_{m,n}} C\mathbf{g_{1,0}^H} & \mathbf{g_{m,n}} C\mathbf{g_{1,1}^H} & \cdots & \mathbf{g_{m,n}} C\mathbf{g_{m,n}^H} \end{bmatrix}. \tag{1.38}$$

Bearing this in mind and taking another perspective: if the steering vector is a linear combination of several modal steering vectors, like in Eq. 1.37, and if we take for example, only 3 steering vectors, it becomes

$$\mathbf{g} = \mathbf{g_1} + \mathbf{g_2} + \mathbf{g_3} \tag{1.39}$$

substituting this in Eq. 1.7 we have

$$b_1 = (\mathbf{g_1} + \mathbf{g_2} + \mathbf{g_3}) C (\mathbf{g_1} + \mathbf{g_2} + \mathbf{g_3})^{\mathbf{H}}$$

$$b_1 = (\mathbf{g_1} + \mathbf{g_2} + \mathbf{g_3}) C (\mathbf{g_1^H} + \mathbf{g_2^H} + \mathbf{g_3^H}) \tag{1.40}$$

and opening the sum we have

$$b_1 = \mathbf{g_1} C \mathbf{g_1^H} + \mathbf{g_1} C \mathbf{g_2^H} + \mathbf{g_1} C \mathbf{g_3^H} + \mathbf{g_2} C \mathbf{g_1^H} + \mathbf{g_2} C \mathbf{g_2^H} + \mathbf{g_2} C \mathbf{g_3^H} \ldots$$
$$+ \mathbf{g_3} C \mathbf{g_1^H} + \mathbf{g_3} C \mathbf{g_2^H} + \mathbf{g_3} C \mathbf{g_3^H}. \tag{1.41}$$

However, if we think of beamforming as a linear operator, since $T[u+v] = T[u]+T[v]$ where u and v are arbitrary vectors and $T[\cdot]$ is an arbitrary linear operator, the beamforming output as a result of a sum of steering vectors would give

$$b_2 = \mathbf{g_1} C \mathbf{g_1^H} + \mathbf{g_2} C \mathbf{g_2^H} + \mathbf{g_3} C \mathbf{g_3^H}. \tag{1.42}$$

Clearly Eqs. 1.41 and 1.42 are not the same. The solution adopted was consider that in fact the beamforming process is a linear combination of every single modal beamforming map, i.e., the final beamforming map can be generated by a double sum of (m,n) beamformings map for each single mode.

As a consequence, assuming modes mutually orthogonal implies that the elements of $\mathbf{B_{modes}}$ away from the main diagonal are theoretically zero, suggesting that duct beamforming reduces to a double sum of (m,n) independent beamforming maps, one for each singular modal steering vector. Acoustic mode by mode maps may be computed together with their allied singular mode power at each frequency obtained by integration over each correspondent map, i.e., the elements on the diagonal of Eq. 1.38.

2 SIGNAL PROCESSING TECHNIQUES

Chapter 1 described all the necessary background theory to compute the correct steering vector for the duct-beamforming technique. Moreover, some concepts like mode propagation within ducts were also introduced.

For the free-field case and spatially stationary sources, the computation of the cross-spectral density matrix can be directly estimated. However, to obtain the cross-spectral density matrix correctly for fan noise analysis, signal processing techniques are required. They include fan harmonic tone removal, the use of virtual rotating microphones; data sampling rate changes and last but not least, adequate spectral estimation. A brief review of the techniques employed here are described next.

2.1 TONE REMOVAL

A spinning fan (or a propeller for that matter) generates strong harmonic tones referred to the *blade passing frequencies* or BPF. This phenomenon is due to the periodicity of the blades' wake in the flow. The frequency is easily calculated by $f_{BPF} = f_{fan(RPM)} * B/60$, where $f_{fan(RPM)}$ is the fan speed in RPM and B the number of blades. These tones can be strong enough to allow power leakage onto the estimated spectrum, leading to estimation errors in both magnitude and phase. For the sake of beamforming imaging, it is important to remove those tones from the signal prior to PSD estimation.

To do so the approach used here rests on subtracting a synthesized harmonic sequence from the total signal, i.e., after estimating the allied amplitudes/phases for each harmonic sinusoid, the estimated signal is subtracted from the measurements in the time domain. This contrasts with a commonly adopted practical alternative that processes the data in the frequency domain by averaging the tone peak along its neighboring values, leading to less desirable results.

Consider a signal $x(n)$, $n = [1, ..., L]$ composed by a sinusoidal with a known frequency f_0 but unknown phase ϕ and amplitude A under additive noise $e(n)$

$$x(n) = Asin(2\pi n f_0 + \phi) + e(n)$$

or equavalently

$$x(n) = A_0 cos(2\pi n f_0) + B_0 sin(2\pi n f_0) + e(n) \tag{2.1}$$

where

$$A_0 = Asin(\phi) \quad and \quad B_0 = Acos(\phi)$$

Rearranging Eq. 2.1 in the matrix form we have

$$\begin{bmatrix} cos(2\pi f_0) & sin(2\pi f_0) \\ cos(2\pi.2 f_0) & sin(2\pi.2 f_0) \\ \vdots & \\ \cos(2\pi.L f_0) & sin(2\pi.L f_0) \end{bmatrix} \begin{bmatrix} A_0 \\ B_0 \end{bmatrix} = \begin{bmatrix} x(1) \\ x(2) \\ \vdots \\ x(L) \end{bmatrix} + \begin{bmatrix} e(1) \\ e(2) \\ \vdots \\ e(L) \end{bmatrix} \tag{2.2}$$

or

$$\mathbf{C} \begin{bmatrix} A_0 \\ B_0 \end{bmatrix} = \mathbf{x} + \mathbf{e}$$

The optimal solution that minimizes $\mathbf{e^H e}$, the sum of squared errors, is given by

$$\begin{bmatrix} \hat{A}_0 \\ \hat{B}_0 \end{bmatrix} = (\mathbf{C}^T \mathbf{C})^{-1} \mathbf{C}^T \mathbf{x} \tag{2.3}$$

where $(\mathbf{C}^T \mathbf{C})^{-1} \mathbf{C}^T$ is the pseudo-inverse of the matrix $\mathbf{C}$.

The pure tone

$$\mathbf{C} \begin{bmatrix} \hat{A}_0 \\ \hat{B}_0 \end{bmatrix}$$

is then subtracted from the raw signal $x(n)$, so the tone free signal $\tilde{x}(n)$ is computed by

$$\tilde{x} = x - \mathbf{C} \begin{bmatrix} \hat{A}_0 \\ \hat{B}_0 \end{bmatrix} \tag{2.4}$$

This formulation presumes that the frequency f_0 is well known. To invoke this approach, a high degree of certainty in the f_0 value (error less than 0.1%) is necessary.

To overcome this problem, consider the first estimation of the BPF coming from the fan speed displayed in the monitoring system during the experiment. For example, 4000 RPM. For a 16 bladed rotor, it will produce a $4000 * 16/60 = 1.067\ kHz$ BPF.

A second and better estimation of this frequency can be obtained by a measured acoustic pressure data from one microphone. A long data set, in this work 2^{16} samples, is Fourier transformed and, once in frequency domain, a range of frequencies close to the first BPF is selected and the maximum value of this segment is registered. This maximum value is associated with the first BPF.

In this way, this value gives a second estimation for the frequency f_0. Surely an improved estimation although not yet good enough.

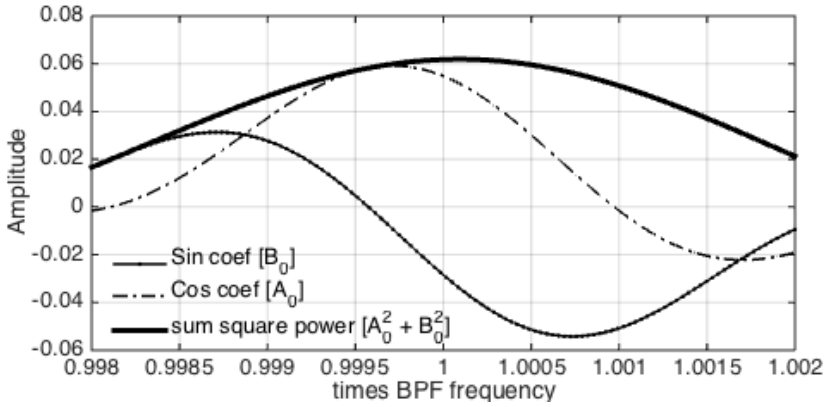

Figure 11 – Coefficients A_0 and B_0 of Eq. 2.3 and the square $A_0^2 + B_0^2$ for an aleatory experiment with fan noise data.

This second estimation of f_{BPF} is used to apply the tone removal introduced above. However, the procedure is repeated about 100 to 150 times around ±0.2% of f_{BPF}. The algorithm performs this search and look for the maximum coefficients of square sines and cosines of Eq. 2.3, i.e., look for $max\{A_0^2 + B_0^2\}$. The maximum is obtained when the frequency matches the real f_{BPF} generated by the fan. A result for this search can be seen in Fig. 11 where the maximum in the power of coefficients is clearly visible.

This maximum is then used as the exact f_{BPF} necessary to remove all tones from all microphone signals. The procedure is repeated until the desired order of BPF. In this work, tones are removed until the 5^{th} harmonic order.

2.2 VIRTUAL ROTATING MICROPHONES - VRM

As introduced in Chapter 1 rotating beamforming requires a rotating reference frame for the formulation of the steering vector. Moreover, the signals from microphones must be spinning at that same speed. Certainly it is not feasible to make microphones spin with the fan. Fortunately, there are some techniques that make the microphones spin virtually, by measurements from microphones at rest.

There are two known different ways to achieve this. It is possible to employ *virtual rotating microphones* as explained by Lowis in (2) and by Pannert *et al.* in (17). The technique proposed by them relies on the frequency shift caused onto the spinning modes.

Briefly, the signal from a ring of microphones is transformed from the time domain to the mode domain, via a spatial Fourier transform. Thus, one can obtain the corrected frequency (shifted) to the corresponding in the rotating frame in frequency domain on a mode by mode basis: $\omega + m\Omega$.

After this correction, the inverse spatial Fourier transform is carried out resulting in the signals of virtually spinning microphones at velocity Ω. Lowis and Pannert demonstrated that this has same effect as if the microphones were rotating around the duct axis at same speed as the fan.

The latter technique was not employed in the present study. For convenience, we opted for using the interpolation technique as described by Herold in (18). A brief introduction of the method is presented as follows, but intuitively it is equivalent to stroboscopically sampling the signals.

The principle behind the interpolation technique consists in creating virtual microphone measurements (i.e., physically do not exist) from static measurements recorded in the circular array. If we fix a rotating point with same speed and direction as the fan, the interpolated sound pressure at this point in a certain time will be the average of the neighboring microphones in the wall-mounted array, weighted by its angular spacing from that point to the microphones, just as a linear interpolation.

Mathematically speaking, let N_c be the number of equally spaced microphones on a ring and $p_m(t)$ be the measured sound pressure in the m-th microphone ($m = 1, ..., N_c$).

The angle α between each microphone is given by $\alpha = 2\pi/N_c$.

If we define the time-dependent angle of the measured point $\varphi(t)$ by the angle position from some reference point in the rotating frame at speed Ω, the limit index, lower and upper (m_l and m_u respectively) of the static microphone signals in which we can interpolate is calculated by

$$m_l(m,t) = \left\lfloor m + \frac{\varphi(t)}{\alpha} - 1 \right\rfloor mod\, N_c + 1 \tag{2.5a}$$

$$m_u(m,t) = \left\lfloor m + \frac{\varphi(t)}{\alpha} \right\rfloor mod\, N_c + 1 \tag{2.5b}$$

where $\lfloor\cdot\rfloor$ denotes the floor function and "*mod*" is the congruence operator. Thus, the weighting factors for the respective sound pressures are given by

$$s_u(t) = \frac{\varphi(t)}{\alpha} - \left\lfloor \frac{\varphi(t)}{\alpha} \right\rfloor \tag{2.6a}$$

$$s_l(t) = 1 - s_u(t) \tag{2.6b}$$

Finally, the interpolated microphone signals $p_{\Omega,m}$ in the rotating frame are calculated by

$$p_{\Omega,m}(t) = s_l p_{m_l} + s_u p_{m_u} \tag{2.7}$$

Once calculated, the virtual rotating signal $p_{\Omega,m}(t)$ is then synchronized with same speed with respect to the fan about an axis of interest. The CSM for the virtual rotating array is then estimated equivalently to the stationary case from the $p_{\Omega,m}(t)$ signals.

2.3 DATA RESAMPLING

Ideally, the best way to acquire acoustic data for fan noise analysis is a data acquisition system triggered to the fan speed via an encoder attached to the shaft (4). Many acoustic sources produced by rotating sources, a fan for example, have their frequency dependent

on the shaft speed, i.e., most of noise sources are frequency multiples of the shaft speed, hence, the BPF.

In this way, if the data is acquired synchronously with the shaft speed, for example 512 samples per fan revolution, the frequencies of these sources correspond exactly in the estimated spectral bins, if used as usual a power of 2 data tapper.

But, if no shaft-sync data acquisition is available, data resampling can be performed to simulate the same effect. This is done in order to give an exact number of samples per revolution. In this work, for convenience, that data was resampled to give 512 samples per fan revolution. To do so a sensor attached to the shaft was used to provide 1 pulse per fan revolution.

Furthermore, when the PSD is estimated from data synced with the fan speed, for a given data window length, the BPF harmonics always match the same bins in the frequency axis. For example, given a 2048 sample data window and 512 samples per revolution sample rate, the PSD's frequency axis (with 1024 bins from 0 to $fs/2$ where fs is the sample rate, $fs = 512 * \text{shaftspeed}$) always has in the $(64+1)^{th}$ position for the 1^{st} BPF, $(128+1)^{th}$ position corresponds to 2^{nd} BPF and so on.

2.4 POWER SPECTRAL DENSITY (PSD) ESTIMATION

The beamforming technique relies directly on PSD estimation, which is an important preliminary step to achieve the final acoustic map. Pressure signals coming from all microphones in the array are processed to produce the cross-spectral density where from beamforming can be computed. One must, however, keep in mind the several practical limitations of spectral estimation methods that vary according to the signal characteristics that lead to like power leakage, spectral blurring, bias, and so on (13–15).

Aeroacoustic noise signals (19) possess continuous spectra derived due to their nature as regular stochastic processes, i.e. without strictly sinusoidal tones. This is in contrast to problems, for example, regarding the electrical power networks whose signals are mostly comprised of 60 Hz and its harmonics.

Our acoustic data acquisition experiments usually have consisted of 30 seconds of

acquired data. It allows for the comfortable use of the well known Welch spectral estimation method (14), in which, as is customary in the literature (13), to adopt 50 % of overlap between signal segments before averaging the absolute squared value of the transforms for each data subsegment to obtain the spectral density estimate. The Hanning window (14, 19) was used throughout, as it is the most popular data window due to its good trade-off between main-lobe aperture and reduced side-lobe levels.

On applying windows in the case of continuous spectra, careful normalization is required to ensure that the power computed over time is the same as the one that would be obtained integrating the spectrum. If the spectrum contains pure sinusoids, the required normalization is different from that of a continuous spectrum leading to some prevailing confusion (20). Because BPFs were extracted from the data, we strictly employed the continuous spectral data window normalization here.

2.4.1 PSD Estimation Details

Let two data records of two signals $\mathbf{x}$ and $\mathbf{y}$ of length comprising N samples, be broken into blocks $\mathbf{x}^{(k)}$ and $\mathbf{y}^{(k)}$ of size L

$$\hat{S}_{xy}^{(k)}(f) = \frac{2 \cdot \mathscr{F}(\mathbf{x^{(k)}} \cdot \mathbf{w}) \cdot conj(\mathscr{F}(\mathbf{y^{(k)}} \cdot \mathbf{w}))}{\sum w_i^2} \tag{2.8}$$

where $\mathbf{w} = [w_1 \dots w_i \dots w_L]^T$ is a suitable data taper window of length L (usually Hanning window (19)). The symbol $\mathscr{F}\{\cdot\}$ stands for the discrete time Fourier transform computed at suitable frequencies f between 0 and one half the Nyquist frequency. The factor 2 comes from using a single-sided representation (positive frequencies only) of the spectrum.

Finally, the cross-spectrum is given by averaging the terms in

$$\hat{S}_{xy}(f) = \sum_{k=1}^{N/L} \frac{\hat{S}_{xy}^{(k)}}{N/L} \tag{2.9}$$

For the cross-spectral matrix, all pairwise microphone combinations must be performed. For example, at a given frequency f_0, the corresponding position of the CSM is given

by

$$\left[C(f_0)\right]_{NxN} = \begin{bmatrix} S_{11}(f_0) & S_{12}(f_0) & \cdots & S_{1N}(f_0) \\ S_{21}(f_0) & S_{22}(f_0) & \cdots & S_{2N}(f_0) \\ \vdots & \vdots & \ddots & \vdots \\ S_{N1}(f_0) & S_{N2}(f_0) & \cdots & S_{NN}(f_0) \end{bmatrix}_{NxN} . \tag{2.10}$$

The term position is used because the CSM is three-dimensional with size $[N\,x\,N\,x(L/2)]$, where L is the data taper length. Commonly the depth of this matrix corresponds to one frequency, and a position of $[N\,x\,N]$ will have all microphones cross-spectra combinations at that frequency, as in Eq. 2.10 for $f = f_0$.

3 EXPERIMENTAL SETUP

This study used two different experimental setups for analysis and comparisons: one constructed at the University of São Paulo, at the São Carlos campus and the ANCF rig at the NASA-Glenn Research Center - USA whose use was was granted via a research partnership between USP and NASA-Glenn allowing data exchange and access to technical details.

This section describes the specifications of both fan rigs.

3.1 UNIVERSITY OF SÃO PAULO (USP) FAN RIG TEST FACILITY

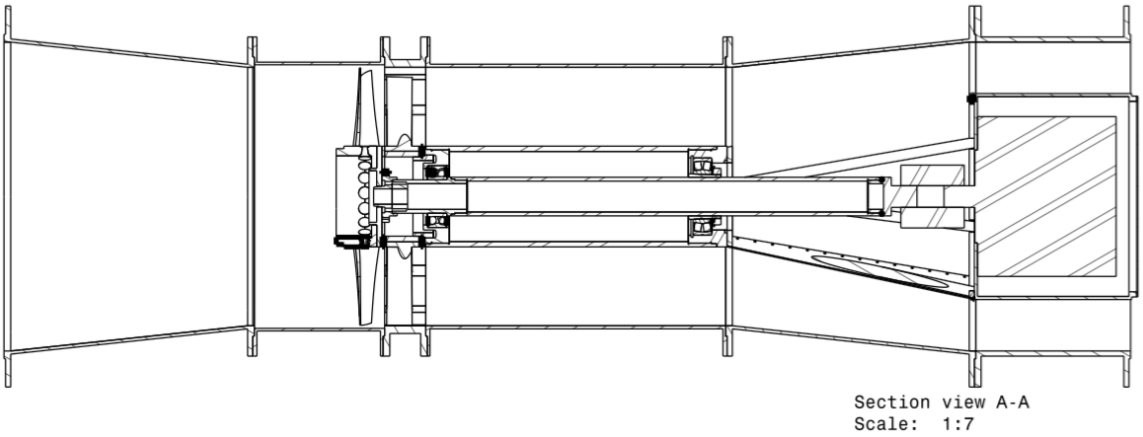

Figure 12 – Motor section details.

The USP rig is a long-duct low-speed fan rig test facility constructed to provide a means for experimentally studying the fluid dynamic details of fan noise generation mechanisms. The rig's configuration was designed with flexibility in mind and allows rig section replacement to suit specific experimental needs.

The rig has a diameter 0.6 m and is about 12 m long; its basic configuration comprises a 0.5 m diameter duct fan stage equipped with a 16-bladed rotor and a 14-vaned stator, as depicted in Figs. 12, 13, 14, 15 and 16. The rotor is powered by an 100HP electrical motor mounted with help of 3 struts that allows experiments up to 4250 RPM and Mach 0.1 flow

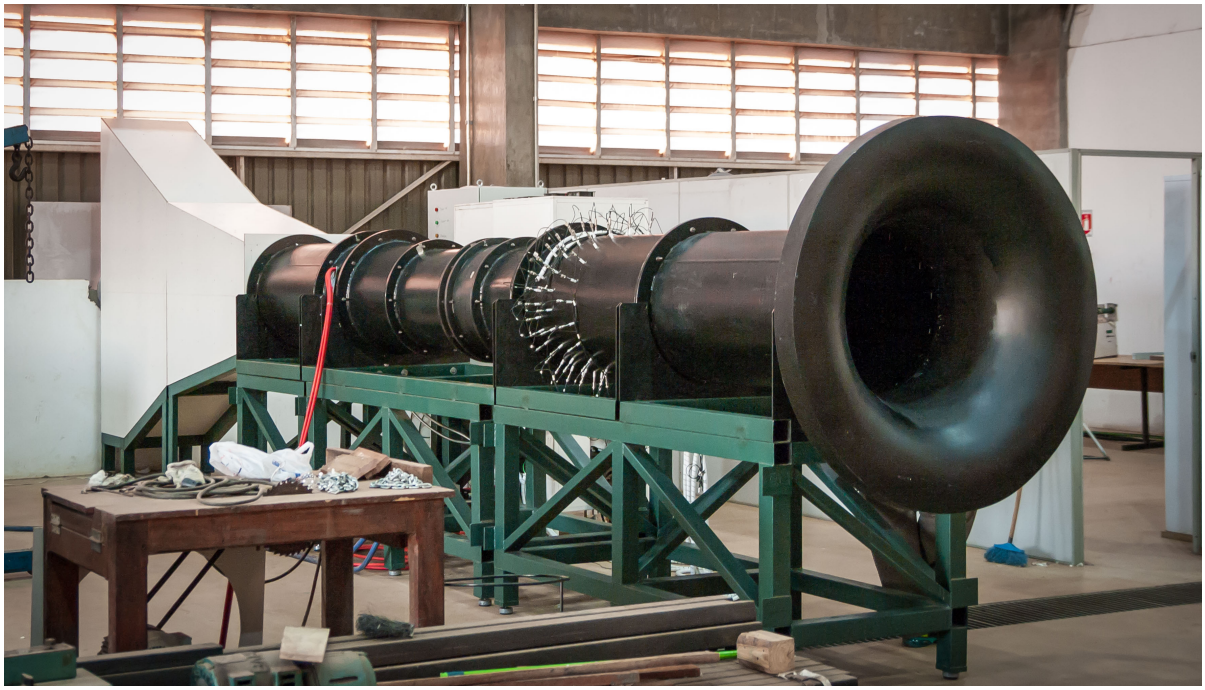

Figure 13 – USP fan rig. Overall view with anechoic termination and bell-mouth inlet.

Figure 14 – Details of the 0.5 m diameter rotor.

speed. Its long duct configuration is similar to that of DLR low speed fan rig (21) and yet differs from other rigs that operate inside anechoic chambers (4, 6, 22).

3.1.1 Antenna design

Microphone duct-array design must take into account some important aspects, namely: bandwidth; distance from the focal plane; duct diameter; number of sensors; number of fan blades and stator vanes. Unfortunately, there are few references to that can

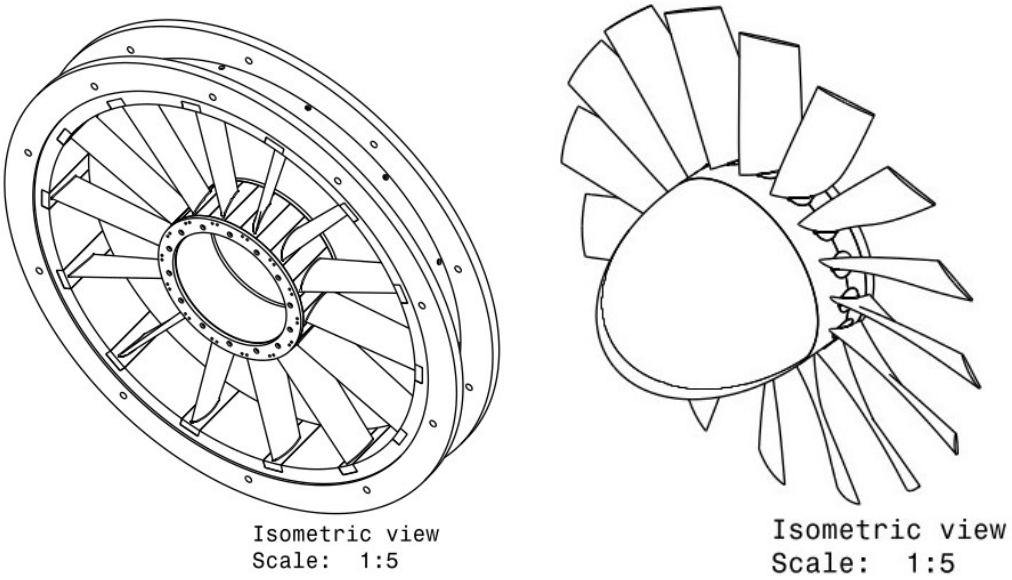

(a) 14-vaned stator (b) 16-bladed rotor

Figure 15 – Details of the pair rotor and stator used in the USP fan rig.

be used as guidelines. Notable exceptions are represented by $(2,4,6)$.

It is known that the total length of the array directly influences the PSF beam-width and side-lobes. Longer arrays have better focus-depth relationship at the expense of a loss in coherence between rings. This calls for a trade-off that must be sought for this array parameter.

The number of microphones per ring depends directly on the maximum circumferential-mode order of interest, according to the Nyquist criteria: $-N_c/2+1 < m_\theta < N_c/2-1$, where N_c is the number of microphones in the ring and m_θ the maximum circumferential-mode order that the array is able to detect without aliasing. Furthermore, Tyler-Sofrin modes can be used as reference to predict the highest order mode as a function of the number of fan blades and stator vanes.

The first big issue in this project was to design the optimal array geometry for rotating beamforming and mode detection. The first attempted configuration was a 4-ring one, comprising 16 mics each, as seen in Fig. 18. We believed that, with a longer array, more rings and fewer microphones per ring, we could increase the array's capability to distinguish close sources, i.e., its beam width would be smaller. However, Lowis (2) has shown that optimal performance is achieved with 3 rings even with a limited number of microphones available

(a) (b)

Figure 16 – Backside view: (a) Close-up in the rotor-stator stage and (b) the end of the rotor stage with 3 struts supporting the motor and the aerodynamic termination.

(around 100). In fact, it is far more important to have a minimum number of sensors per ring (in this case, more than 20 sensors per ring) than to have a large number of rings.

In the first array (see Fig. 18) theoretically only modes up to $m = \pm 7$ could be detected which is insufficient for reasonable characterization of fan broadband noise. Furthermore, beamforming map artifacts occur in a circumferentially symmetric pattern that is a multiple of the number of sensors at each ring. So, for a fan with 16 blades and an array with 16 sensors per ring, artifacts with a 16 pattern would be undesirably jumbled with a possible noise coming from the blades.

For these reasons a second version of the microphone array was introduced. The solution was to reduce the number of rings and increase the number of sensors per ring. The total array length went from 0.42 m to 0.27 m in the final array version and an odd number of microphones was used per ring. This last solution was adopted to avoid artifacts in the form of multiples of the number blades on the beamforming map and to allow the easy distinction of artifacts from fan or stator noise.

Finally, as the number available of microphones was limited, each ring was endowed with a different number of microphones. A ring with larger number of sensors closer to the focal plane is highly recommended to facilitate the detection of higher order modes.

Moreover, (5) observed that aligned microphone pairs were far more correlated than pairs corresponding to different angles. It is believed that the cause is convected boundary layer turbulence: two microphones experience nearly the same turbulence if they are aligned stream-wise leading to a rule aligned microphone designs should be avoided. Also the use of different numbers of microphones per ring contributes to avoid the repetition of the distances between microphones much like in non-periodic plane arrays (23).

Fig. 19 shows the second array designed. It has three separate rings 0.10 and 0.17 m apart, each ring comprising 33, 23 and 21 uniformly distributed microphones.

(a) Blade's upper surface (b) Blade's trailing edge (c) Vane's upper surface (d) Vane's leading edge

Figure 17 – Blade e vane of the USP fan rig.

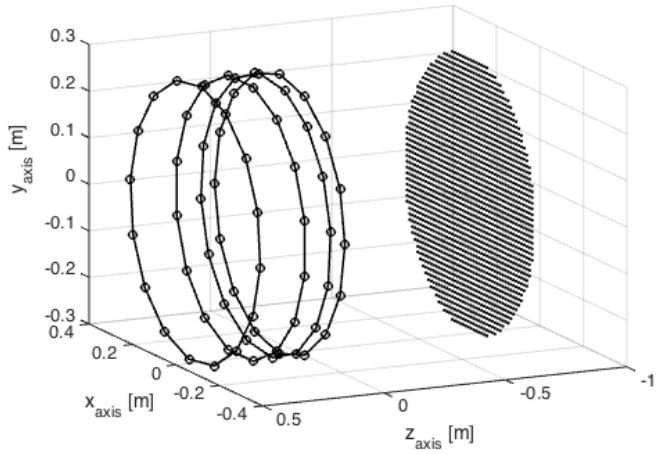

(a) 64-mic array (circles) and the focal plane represented by the black dots.

(b) Microphones mounted.

Figure 18 – First antenna used with 4-rings and 64-microphones.

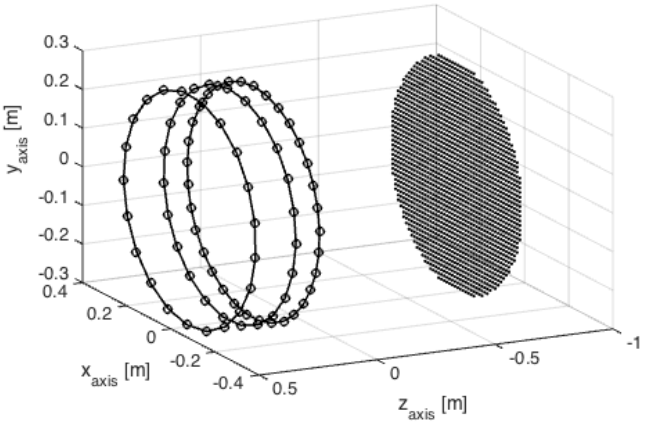

(a) 77-mic array (circles) and the focal plane represented by the black dots.

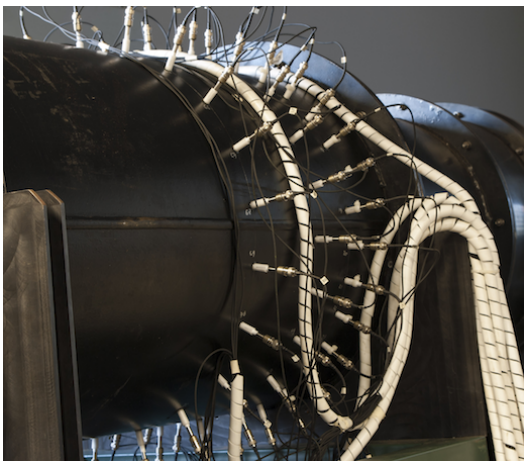

(b) Microphones mounted.

Figure 19 – Second antenna composed by 3-rings with 77-microphones in total.

3.1.2 Acoustic data acquisition system

The acoustic data acquisition system comprises flush-mounted microphones (GRAS 40PH-S2 ϕ $7mm$, bandwidth of 20 to 20 kHz and 50 mV/Pa average sensitivity) operated via a PXI National Instruments system composed of 5 PXI-4496 boards. Angular motor position is also simultaneously acquired.

3.1.3 Blade trip strip

Following (24) section 7.3: "A more complex form of lock-in that can occur in low-speed fans is called *laminar boundary layer-wake interaction*. Qualitatively speaking, periodic shear layer velocity perturbations, due to Tollmein-Schlichting waves and hairpin vortices, occur during the transition from laminar-to-turbulent boundary layer flow on rotor blades when the Reynolds number based on the chord length is in the approximate range $10^5 < UC/\nu < 10^6$, where U is the velocity at the leading edge of the blade. If the frequency of these periodic shear layer instabilities matches the frequency of vortex shedding, then a hydrodynamic lock-in phenomenon takes place. This causes the periodicity in the wake of the blade to be amplified. If these vortex frequencies happen to be near a harmonic of the BPF, then significant increases in the sound at this frequency will occur." Since the USP fan rig operates in a similar situation, a trip strip was used to force the shear layer transition from laminar to turbulent at the same blade position. Without the boundary layer trip strips the shape of the blade wakes (depth and width) varied significantly from blade to blade. This caused the energy to change from BPF to lower shaft orders and into the broadband.

The necessary trip length was estimated using Pope (25) as reference. Calculations are highlighted on Table 1.

3.2 ADVANCED NOISE CONTROL FAN - ANCF - NASA GLENN

Data from a second fan rig test facility was used to perform algorithm validation and for result comparison. The ANCF at NASA Glenn is a short-duct low-speed fan rig as described in (22) and (26). It is 1.22 m in diameter. The hub is 0.457 m at the fan and 0.61 m aft portion of the duct, as shown in Figs. 20, 21 and 22. The rotor and the stator have the same geometry and blade/vane count as the USP fan rig even though the ANCF is larger. It is powered by an electrical motor fixed outside the duct allowing it to achieve speeds up to 2000 RPM and Mach 0.13 mean axial flow speeds.

The 90-microphone duct-array has 3 rings of 30 sensors equally spaced upstream from the rotor, as in Fig. 23. Furthermore, the rig has a rotating-rake antenna with 5 micro-

Table 1 – Fan rig parameters for trip-strip height estimation

	Meters	Imperial (Feet)
1 m to	1	3.28
Blade chord	0.057	0.187
Blade span	0.25	0.82
Speed (RPM)	4250	4250
Speed (70% span)	77.9 m/s	256 feet/s
Sound speed	355	1164
Mach# @blade	0.17	0.17
Air flow	60.4	198
U total(70% span)	98.5	323
Air kin. Visc.	15.7μ	169μ
Reynolds	$358k$	$358k$
Re effective	$6.28M$	$1.92M$
LE-to-trip (%Chord)	5%	5%
Re (LE-to-trip)	$17.9k$	$17.9k$
Constant K	—	1000
trip height	**0.16mm**	**6.26mInch**

phones in the radial direction placed just on the inlet. The rake spins at $1/100\,th$ the speed of the fan and is used for mode detection.

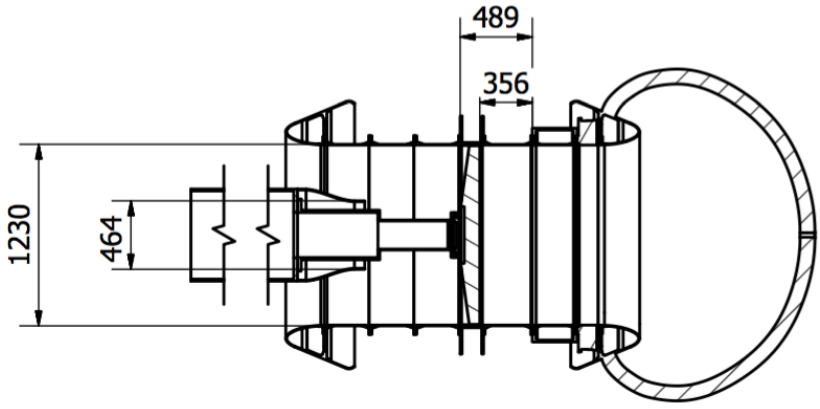

Figure 20 – ANCF technical draw. Units in mm

In Fig. 21 the duct inlet is hidden behind the *inlet control device* (ICD). The first blue section after that, contains a 90-microphone array. Downstream, the gray section there are 2 rings of 16 speakers each surrounding the duct. These speakers are used to generate artificial modes up to $m = \pm 6$. Finally, the next dark-blue section comprises the 16-blade rotor.

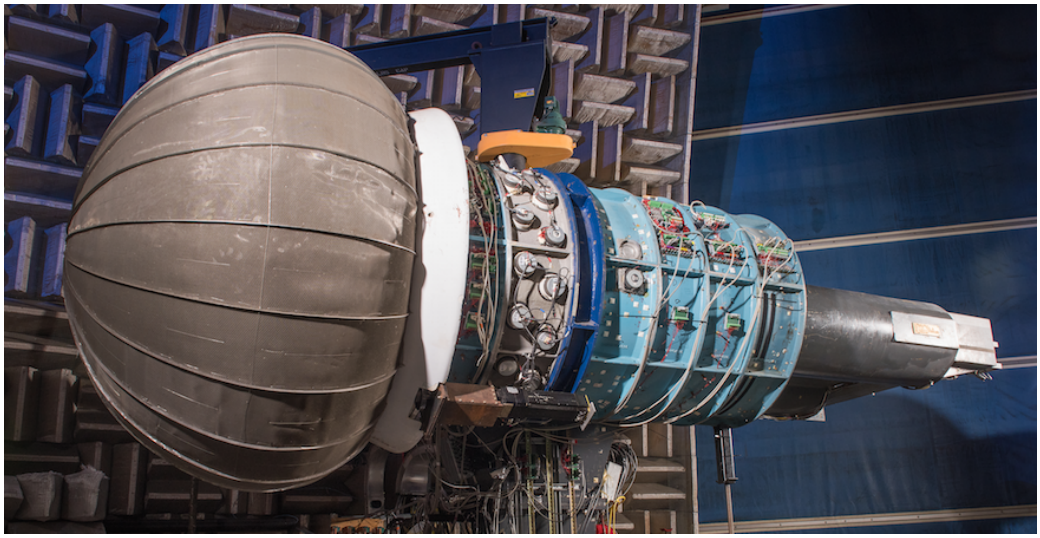

Figure 21 – ANCF: side view. Inlet hidden by the ICD. Microphones array in the downstream section after the ICD followed by the duct-speakers section for artificial noise generation.

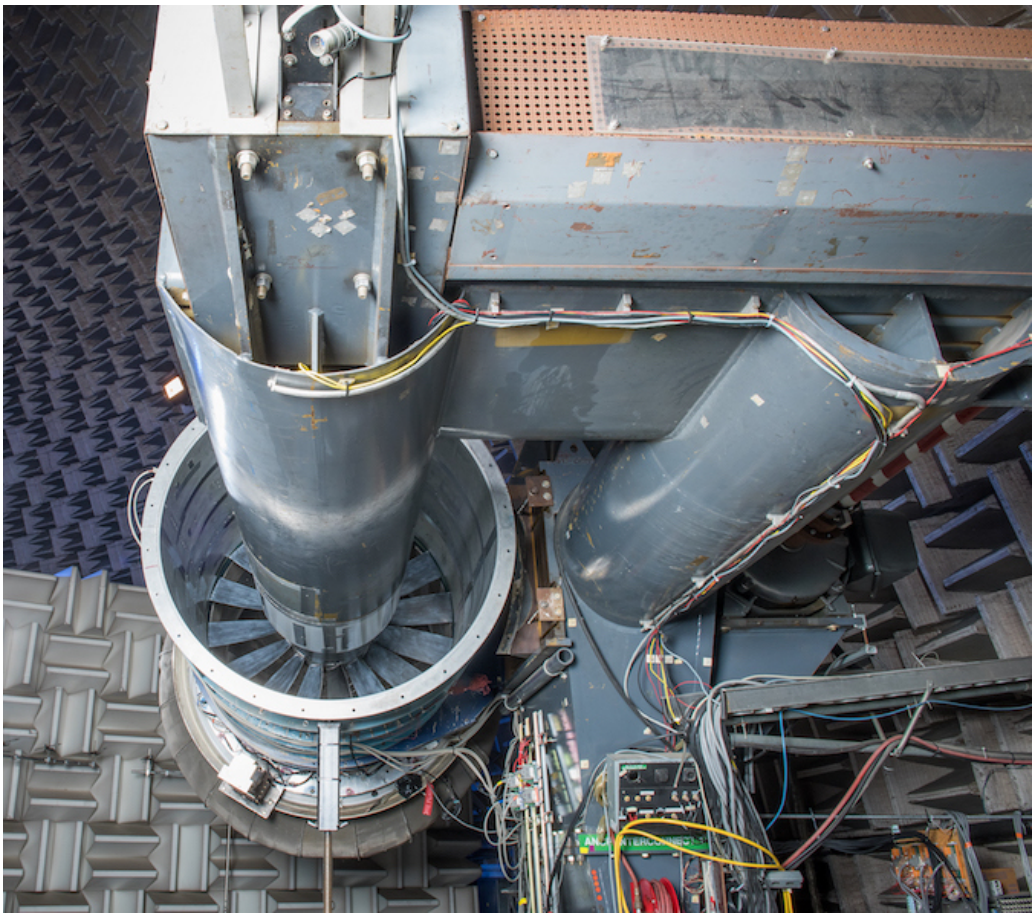

Figure 22 – ANCF: back view. The fan can be seen within the duct. In the right side of the duct is the pylon supporting all the structure.

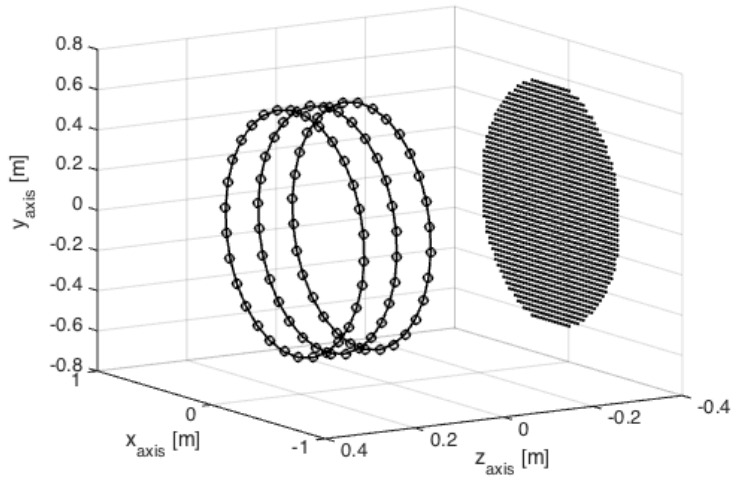

Figure 23 – 90-mic array (circles) and the focal plane represented by the black dots.

4 BEAMFORMING SOFTWARE

The in-house developed beamforming software is based on all formulations presented in Chapters 1 and 2. As introduced in Chapter 1, we adopted the modal steering vectors based on Bessel functions of the first kind which is the solution for a circular duct section.

However, a quite more complex geometry is observed on the travel path from the rotor to the microphones section, such as: the rotor is an annular section, followed upstream by the spinner (varying annular to circular section), then the conical duct from 0.5 m to 0.6 m and finally the 0.6 m duct section comprising the microphones array. All this is depicted in Fig. 12.

Instead of considering this real and complex acoustic path in the steering vector, we approximated that as a 0.6 m circular constant diameter from the microphone array until the fan rotor. In other words, we did not take in to account the duct contraction (from 0.6 to 0.5 m) neither the circular to annular fan section.

Certainly this approximation can lead to some errors because the acoustic characteristics depend directly on duct diameter as discussed in Chapter 1, so this contraction changes the axial wavelength and the range of cut-on modes. Besides, the Mach number increases about 20% when the flow is compressed at the fan section. This variation can also induce errors in the present formulation.

A summary of typical parameters for both rigs is shown in Table 2.

4.1 BREAKDOWN STRUCTURE

Two block diagrams are displayed to clarify the signal processing workflow: Fig. 24 shows the cross-spectral matrix (CSM) evaluation step with arrows marking signal processing steps towards the three CSM estimated instances:(a) Raw (with no data modification); (b) Static (with tone removal and data resampling) and(c) Rotating (Tone removal, Rotating array and data resampling).

Fig. 25 portrays the data flow for the conventional beamforming algorithm. Its input parameters are listed allowing the user to choose whether to perform rotating or static beamforming. Outputs comprise beamforming maps and modal analysis plots.

An example screen of the running software is shown in Fig. 26 together with typical values for the USP fan rig.

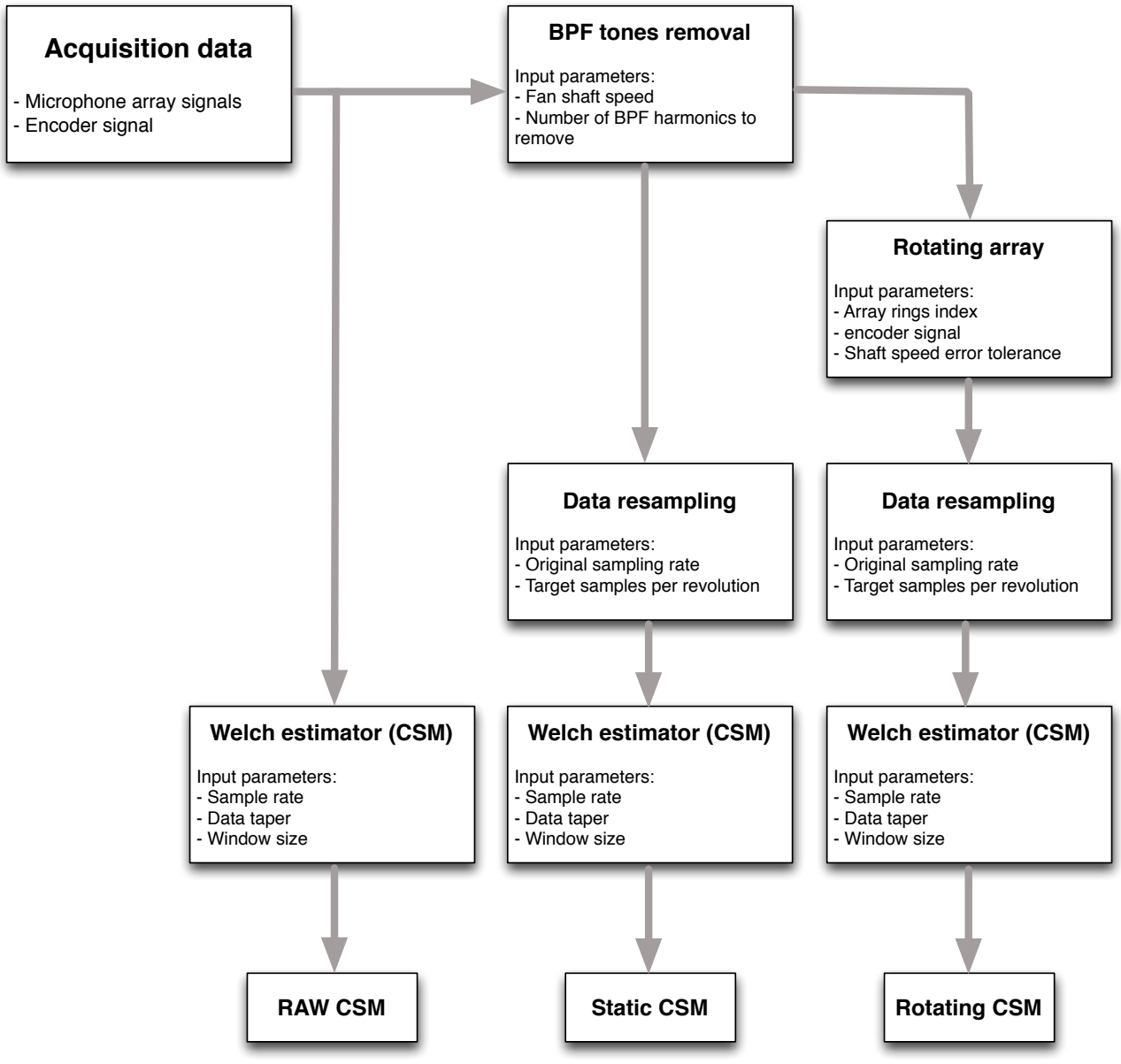

Figure 24 – Cross-spectral matrix (CSM) estimation software breakdown structure.

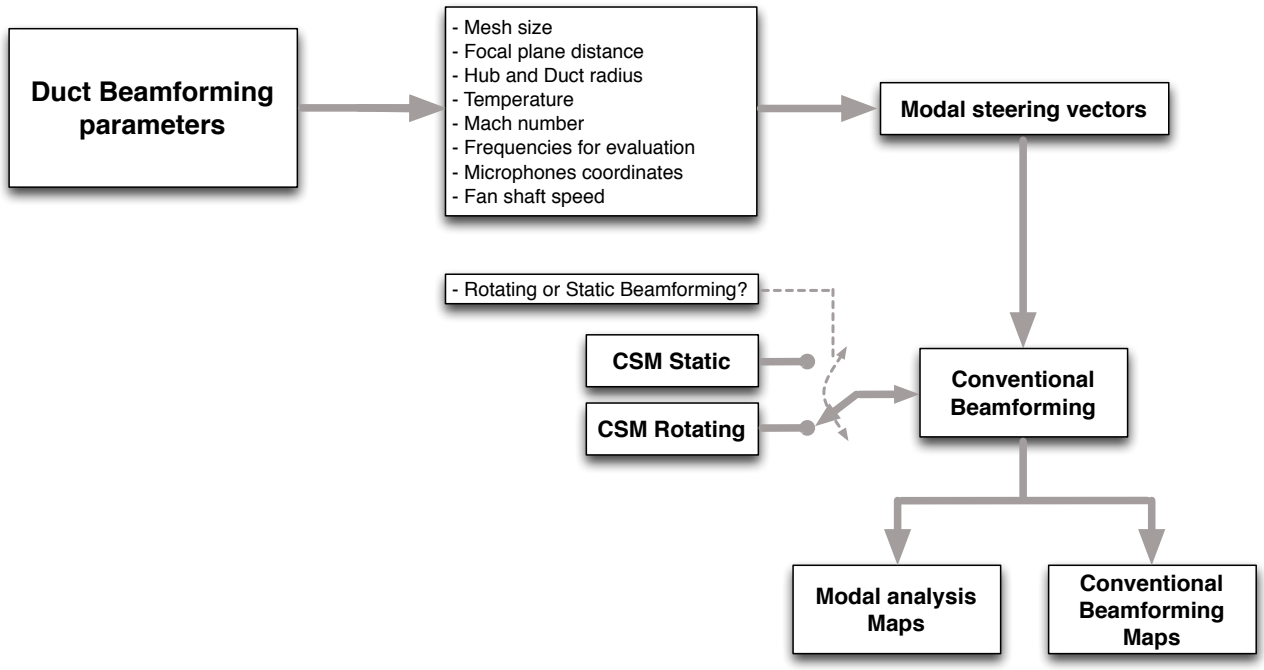

Figure 25 – Conventional beamforming software breakdown structure.

Table 2 – Parameters of both rigs used for beamforming and signal processing

	ANCF-NASA	USP fan rig
Rig parameter		
Duct diameter (m)	1.22	0.6
Fan diameter (m)	1.22	0.5
Hub diameter (m)	0.46	0.19
Hub-to-tip ratio	0.38	0.38
Blades count	16	16
Vanes count	14	14
Max. speed (RPM)	2000	4250
Mach flow max. (inlet)	0.13	0.096
Distance fan to array (m)	0.36	0.71
Number of mics.	90	77
Beamforming param.		
Mesh size (dots)	180×180	180×180
Resolution grid (mm)	6.8	3.3
Spectral analysis param.		
Data taper type	Hanning	Hanning
Data taper length	2048	2048
Re-sampling ratio (S/rev)	512	512
Sampling frequency (S/s)	96k	51.2k
Acquisition time (s)	40	32
Number of BPF to remove	5	5

```
>> Macro_FANRIG_Unix

Starting matlabpool using the 'local' profile ... connected to 8 workers.

CBF_parameters =

                    DuctRadius: 0.3000
                      MeshSize: 180
                     FanRadius: 0.2500
                    FocalPlane: -0.7100
                     RubRadius: 0.1000
                     RunNumber: 1
                   Temperature: 22
                     BeamSpeed: 4250
                    MachNumber: 0.0960
                  DynamicRange: 9
                   Frequencies: [1x1024 double]
               EvaluatingLayers: [1x301 double]
                     SampleRate: ''
    RotatingCrossSpectralMatrix: [77x77x1024 double]
      StaticCrossSpectralMatrix: [77x77x1024 double]
                MicsCoordinates: [77x3 double]
                  ModeDetection: 'n'

Evaluating Conventional Duct-Beamforming
Mach Flow: 0.096
Beam Speed: 4250RPM
Number of Microphones: 77
Sound of speed: 344.406m/s
Mesh grid: 180x180 dots
Duct radius: 0.3m
Focal plane distance: -0.71m
CSM freq layer: 60, 1 of 301, frequency: 1.04e+03Hz, , z_s layer: 1 of 1, time spent: 34.5s
```

Figure 26 – Screen for the beamforming software running with typical parameters for the USP fan rig.

5 EXPERIMENTAL RESULTS

Experimental results from both fan rigs (ANCF-NASA and USP fan rig) are presented here. Even having same rotor/stator geometry but different scales and duct configuration, it is possible to see many differences between the the two set-ups.

All power spectral density (PSD) was obtained by the average of all microphones in the array and displayed in decibel (dB) scale referred to the sound pressure of 20 μPa.

Beamforming maps are in decibel (dB) scale referred to the sound pressure of 20 μPa. A dynamic range of 9 dB was fixed on the plots. The x-axis and y-axis are labeled in meters. On the top of each map the frequency for the evaluation is displayed, along with the Mach flow speed, rotating beamforming beam speed and focal plane distance.

Modal breakdown plots are also in decibel (dB) scale but referred to the sound power of 1 pW. A dynamic range of 12 dB was fixed on the plots.

Due to the great number of experimental results obtained, below a quick summary of all results is listed:

→ Section 5.1: Fan noise power spectra and post processed results that includes: Raw PSD; Tone removal; Virtual rotating microphones.

→ Section 5.2: Results for the mode detection code validation using data from the synthetic mode generator at the ANCF-NASA.

→ Section 5.3: Tyler-sofrin modes were detected for both rigs and were compared for different shaft speeds.

→ Section 5.4: Static and rotating beamforming results for the ANCF-NASA fan rig are displayed. A limitation of the array for mode detection is seen in subsection 5.4.3.

→ Section 5.5: Static and rotating beamforming results are exposed for the USP fan rig test facility. A special test for the rotating beamforming is seen in subsection 5.5.2, where a small device was attached to one single blade in order to increase its noise.

5.1 FAN NOISE POWER SPECTRAL DENSITY

All results for Power spectral density (PSD) displayed in this Section were estimated by the Welch method as described in Section 2.4.1, with 50% overlap, and a Hanning data taper with 2048 samples.

5.1.1 Raw power spectra

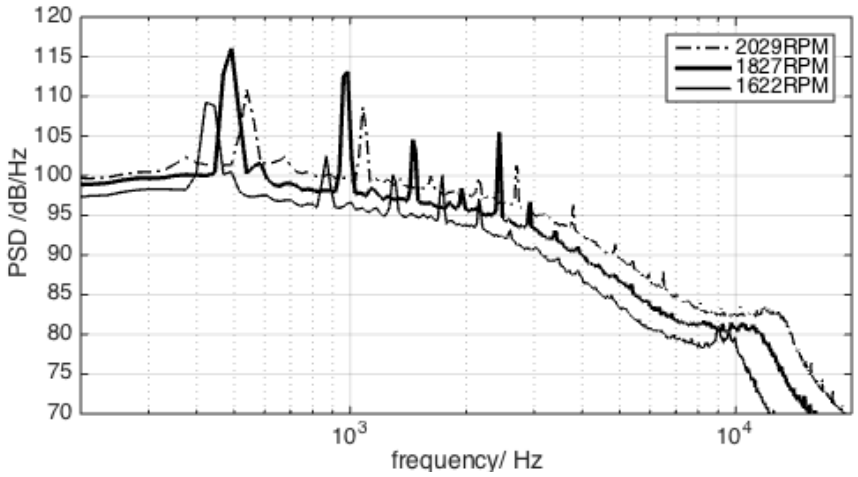

Figure 27 – ANCF-NASA power spectra for three different shaft speeds. Frequency axis in Hertz.

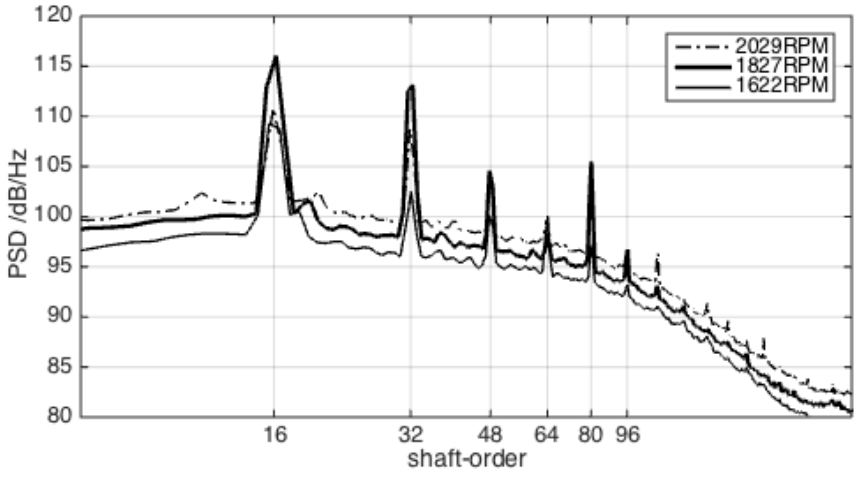

Figure 28 – ANCF-NASA power spectra for three different shaft speeds. Frequency axis in shaft-order.

Baseline power spectra are shown for three different shaft speeds for both rigs. Fig. 27 shows a plot for the ANCF-NASA rig. It is possible to look at the different BPF frequencies as a result of different shaft speeds. Fig. 29 portrait results for the USP fan rig. We can highlight

that the BPF tones are broader in comparison with Fig. 27, i.e., it is not a pure tone. That will be better discussed in next section.

To allow different perspectives, two different frequency axes (x-axis) are used to plot the power spectra. One in Hertz (Figs. 27 and 29), as typical for PSD visualization. A second type is useful for fan noise analysis: shaft-order frequency axis (Figs. 28 and 30), where the frequency axis is normalized by the shaft speed, i.e., the frequency shown on the axis must be multiplied by the actual shaft-speed (in Hz) to obtain the real corresponding frequency. With this representation, all BPF tones always appear at the same shaft-order frequency. For a fan with 16 blades, the first BPF corresponds to the frequency of 16 times the shaft-order.

The use of the shaft-order frequency-axis in contrast to Hertz axis allows us to distinguish noise source generated by mechanisms regarded to shaft frequency speed or other. For example, comparing Fig. 29 with 30 we see that the peak noise between $300-400\,Hz$ is approximately in same frequency in 29, independent of the fan speed. However, in Fig. 30 they no longer match. This is a different phenomenon compared to BPF which is a known tone related to the shaft speed and all tones collapse at same shaft-order frequency. Therefore this noise probably comes from the vibration of the fan rig setup (one of its natural vibration frequencies) and does not depend on shaft speed.

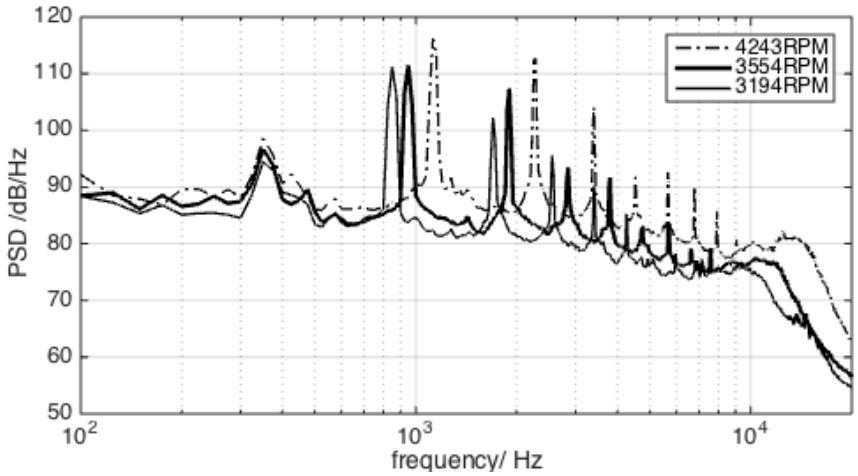

Figure 29 – USP fan rig power spectra for three different shaft speeds. Frequency axis in Hertz.

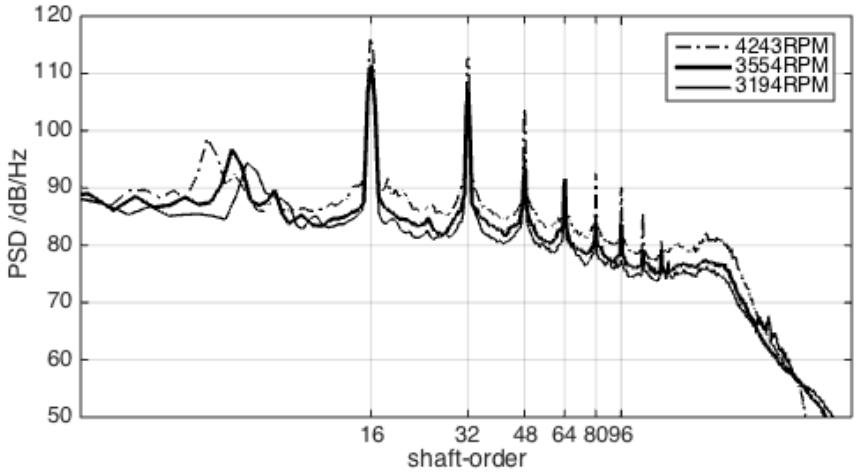

Figure 30 – USP fan rig power spectra for three different shaft speeds. Frequency axis in shaft-order.

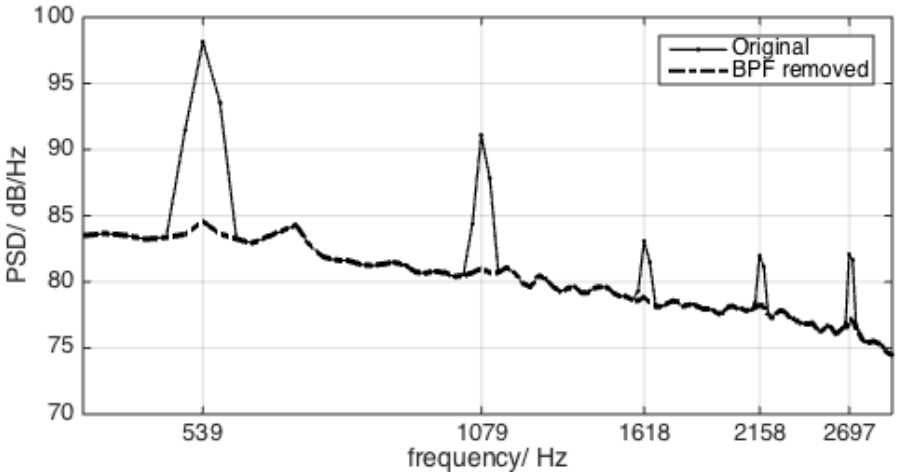

Figure 31 – ACNF power spectra for 2029 RPM with and without BPF tones.

5.1.2 Removed Tones

The first post processing technique performed is the fan tone removal from the broadband power spectra. Results for the ANCF-NASA can be appreciated in Fig. 31 for the fan at 2029 RPM. BPF ticks are marked from the first to fifth harmonics. The results are fairly good, since the tones are esentially pure which allows their removal without problems.

Results for the USP fan rig are seen in Fig. 32. Note that the tones are a little broader at the base, i.e., when the pure sinusoid are removed from the signal, local valleys appear close to the regions of tone removed spectra, revealing that the tones are somehow mixed or modulated by surrounding frequencies.

One possible reason for that happens only in the USP fan rig is the level of turbulence

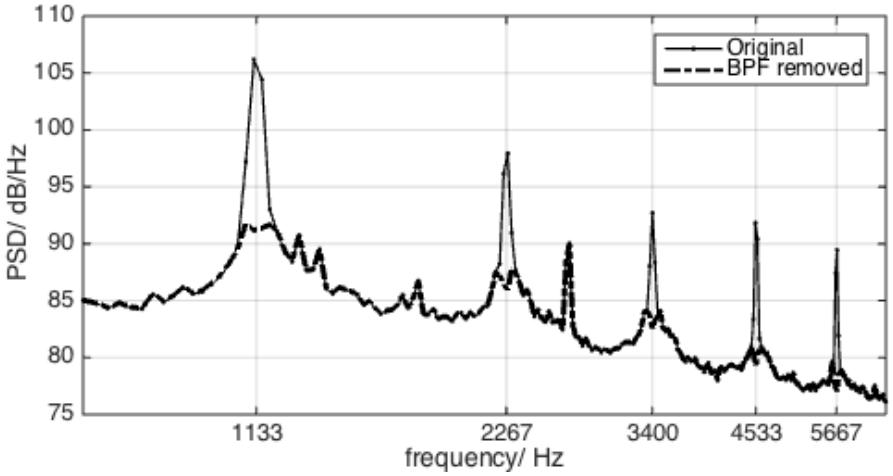

Figure 32 – USP fan rig power spectra for 4250 RPM with and without BPF tones.

ingested by the fan. The ANCF has an ICD (Inlet Control Device, detailed in Section 3) to reduce the flow turbulence levels which comes to the fan, however, the USP fan rig does not have this device. Future experiments with an ICD installed would reveal if that hypothesis is correct. We believe that high turbulence levels can interfere directly with the blade wakes, leading to those impure BPF tones.

5.1.3 Rotating spectra

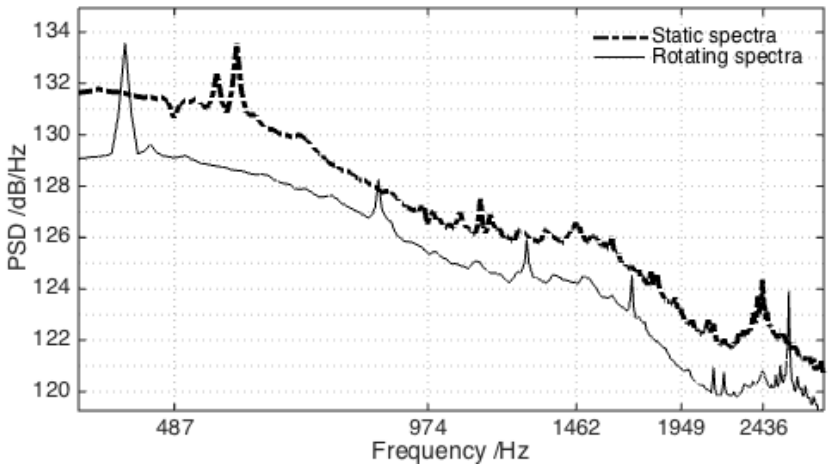

Figure 33 – ACNF-NASA power spectra for static and virtual rotating microphones at shaft speed of 1822 RPM. 1^{st} to 5^{th} BPF sticks are shown.

After BPF tones removal, the rotating microphones technique (as described in Section 2.2) was applied to the array signals. Figs. 33 and 34 show results for both rigs. The rotating power spectra are not commonly seen in the literature. In fact, they are presented

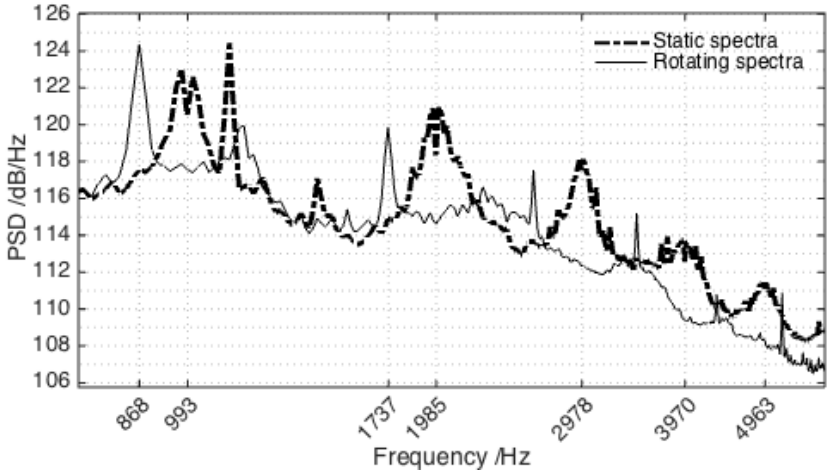

Figure 34 – USP fan rig power spectra for static and virtual rotating microphones at shaft speed of 3722 RPM. 1^{st} to 5^{th} BPF sticks are marked for the static reference frame and 1^{st} to 2^{nd} to the rotating reference frame.

here to illustrate what changes when the frame of reference changes, i.e., when microphones are virtually spinning with the fan.

The shape of the spectra follows the static one. Tone peaks are seen in the rotating PSD for frequencies just bellow the BPF for the static PSD. We believe that their frequency respect to BPF shifted to the rotating frame, just as introduced by Eq. 1.31 in Chapter 1. It is known that modes at BPF are Tyler-Sofrin modes (28), i.e., for the USP fan rig, with 16 blades and 14 stator vanes, the mode $m = +2$ is produced for the first BPF, $m = +4$ for the second and so on. The Tyler-Sofrin mode analysis for that same fan rig was already performed in (27). In this way, the first BPF tone with the fan at 3722 RPM will appear in the rotating frame with the frequency

$$f_1' = 993 - 2 \times 3722/60 = 868$$

and for the second BPF

$$f_2' = 1985 - 4 \times 3722/60 = 1737$$

both seen in Fig. 34.

The difference in the level observed in Fig. 33 was not observed in Fig. 34. Furthermore, the broader region surrounding the BPF tones (Fig. 34) disappear when the VRM (Virtual Rotating Microphones) technique is applied.

5.2 MODE DETECTION: SYNTHETIC MODE GENERATOR AT ANCF-NASA GLENN

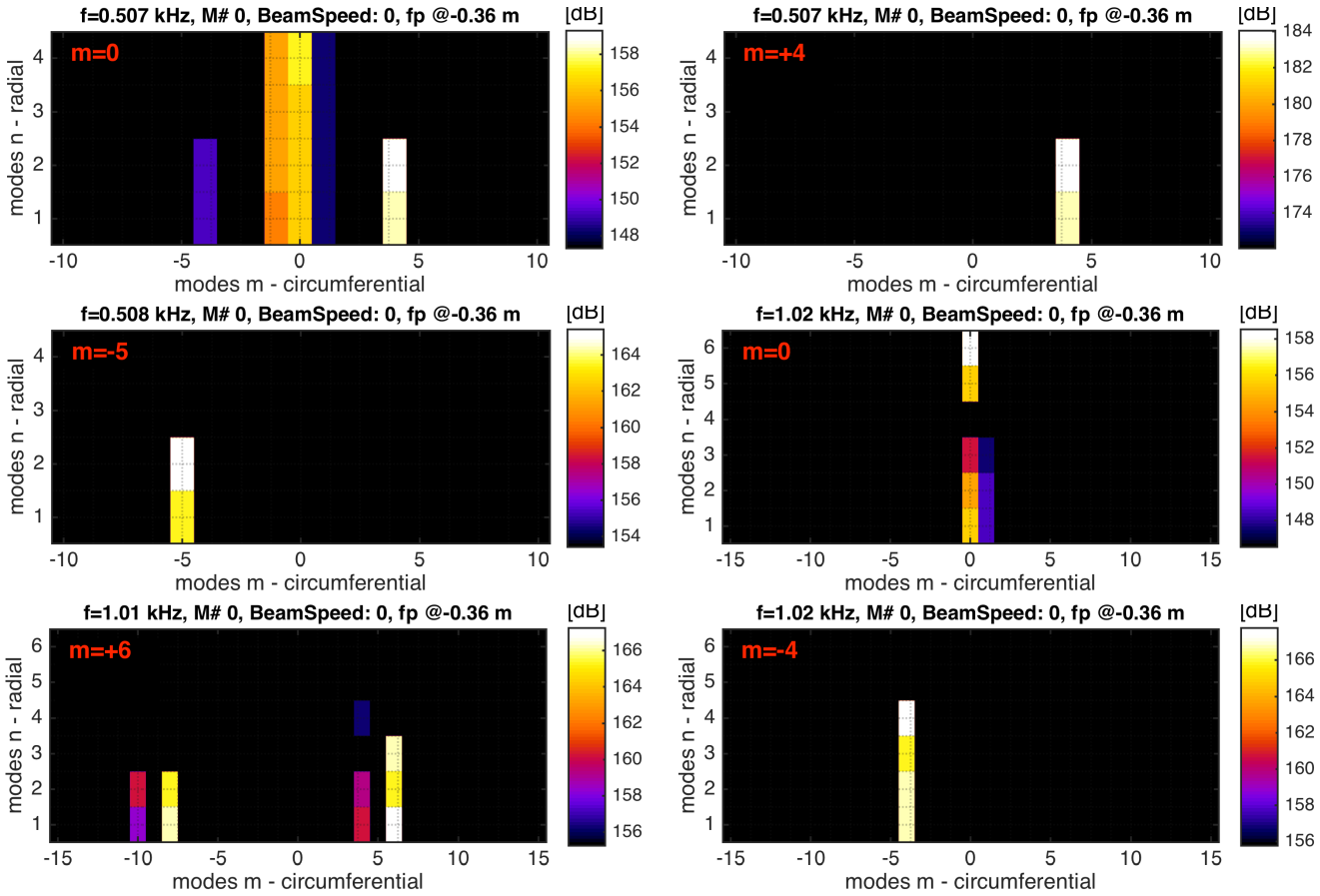

Figure 35 – Modal analysis for the ANCF synthetic mode generator: Left-top tone at 508 Hz and circumferential mode $m = 0$. Right-top 508 Hz and $m = +4$. Mid-left 508 Hz and $m = -5$. Mid-right 1.02 kHz and $m = 0$. Bottom-left 1.01 kHz and $m = +4$. Bottom-right 1.02 kHz and $m = -4$.

An experiment to generate artificial modes using speakers was carried out at the ANCF-NASA center. The data from that experiment were used to validate the code for mode detection. More details about the setup can be seen in Section 3.2 and in (26). Previous results were obtained and were published in (27).

A few cases were selected for illustration purposes. Each is shown on Fig. 35. In all cases the generated mode could be detected correctly, except for the top-left plot where mode $m = 0$ at frequency of 508 Hz was not the maximum mode detected. There are two possible reasons for that: One is that the array was too close to the speakers not allowing enough distance for shape constitution. A second possibility derived from observing many

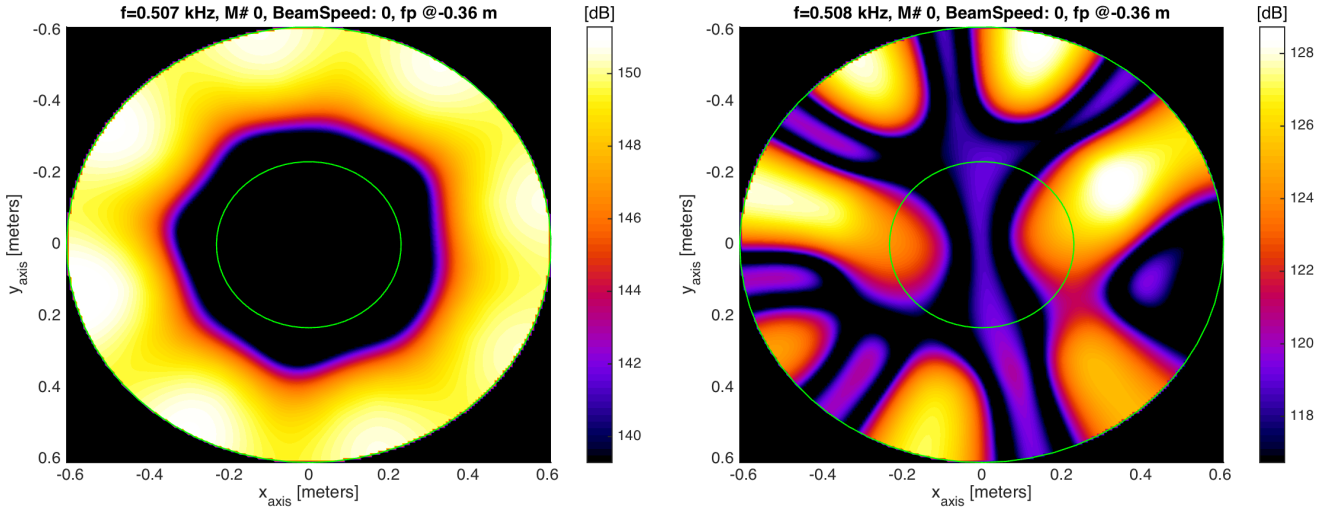

Figure 36 – Conventional beamforming for the synthetic mode generator. Both for 507 Hz. Left is mode $m = +4$ and right $m = -5$.

other experiments, is that the $m = +4$ mode fits very well in the duct geometry and it is easily excited. The exact reason for this remains obscure.

Two mode shapes are displayed in Fig. 36. The beamforming map was obtained with same data as in Fig. 35. The number of maxima in the image match the mode order. For the left map, $m = +4$, we can see 8 equally spaced maxima in the circumferential direction. On right map this is not as clear. Possibly the mode is not pure and what we see is a combination of more than one single mode.

5.3 TYLER-SOFRIN MODES

Tyler-Sofrin modes (28) are generated by the interaction between rotor blades and stator vanes that can be detected at BPF harmonics. These tones are quite strong compared to the broadband level and modes associated with that are important to be detected. Some research is focused on reducing only the tonal noise in order to reduce the total noise produced by the fan (29, 30). Certainly, for this research focus, the Tyler-Sofrin mode detection is quite important.

The expression for the expected mode interaction is given by $m = nB + kV$ where B is the blade count, V the vane count and (n, k) can be any integer $(3, 28)$. The modes observed in Fig. 37 and 38 are obtained, for the first BPF, by $m = 1 \times 16 - 1 \times 14 = +2$.

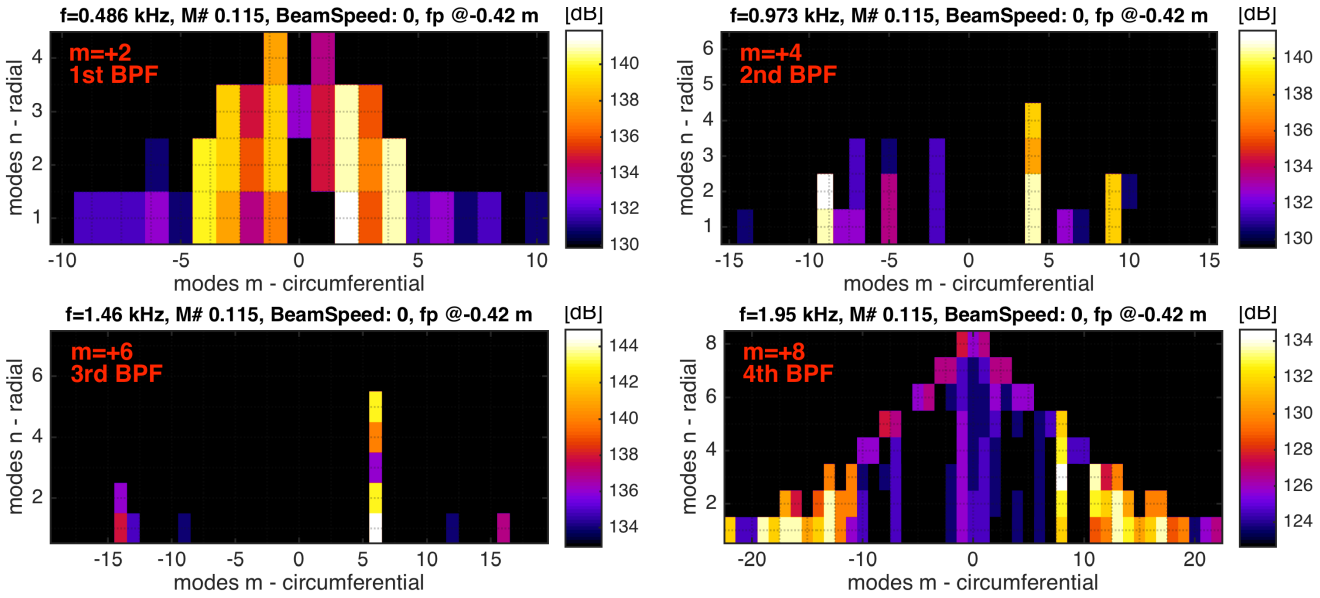

Figure 37 – ANCF-NASA Tyler-Sofrin modes detected. Fan at 1822 RPM with mach flow M=0.115. First to fourth BPF are shown.

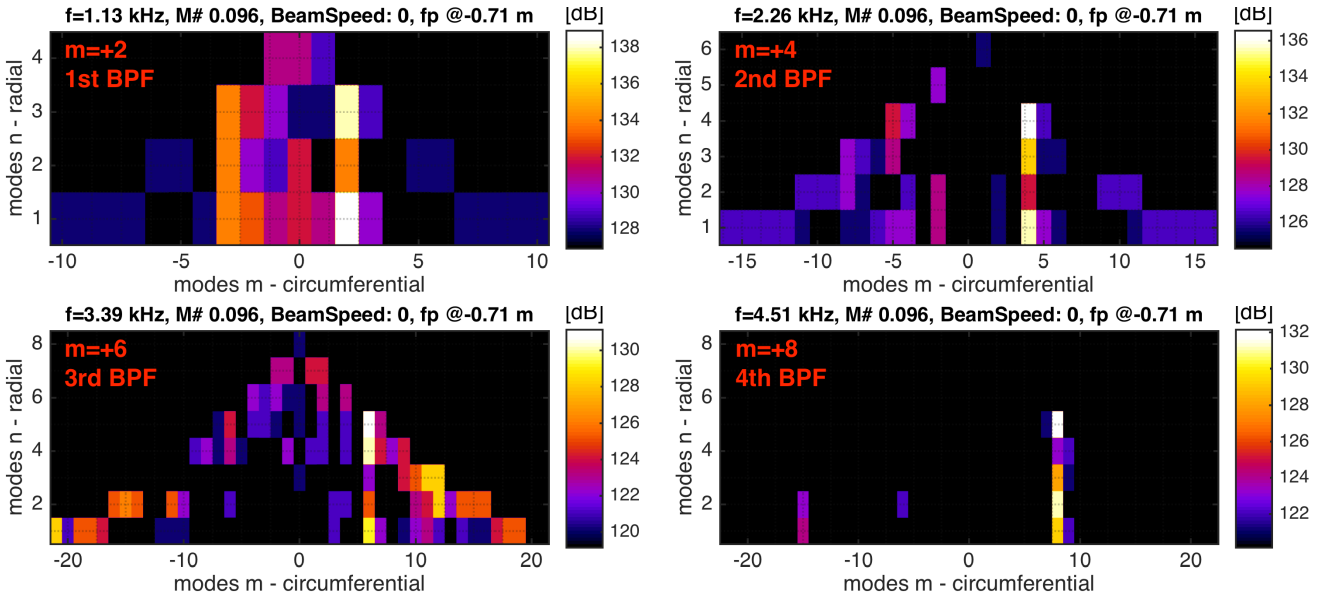

Figure 38 – USP fan rig Tyler-Sofrin modes detected. Fan at 4243 RPM with mach flow M=0.096. First to fourth BPF are shown.

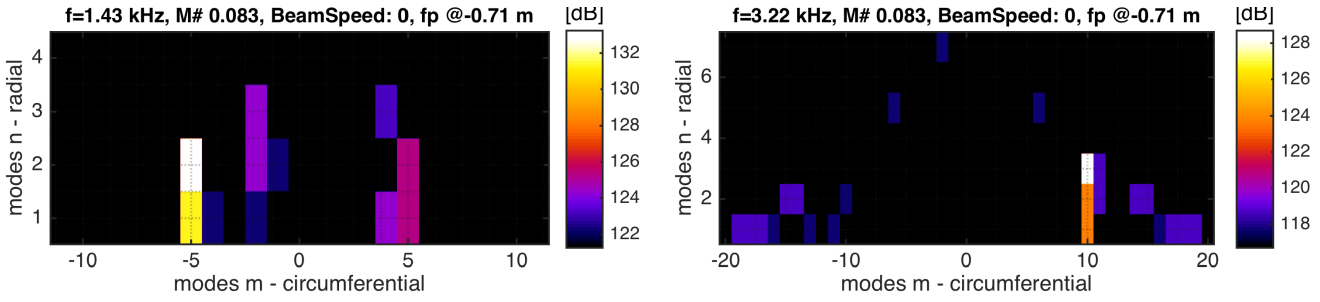

Figure 39 – USP fan rig Tyler-Sofrin modes detected. Fan at 3722 RPM with mach flow M=0.083. Left plot at 1.44 BPF and Right plot at 3.24 BPF.

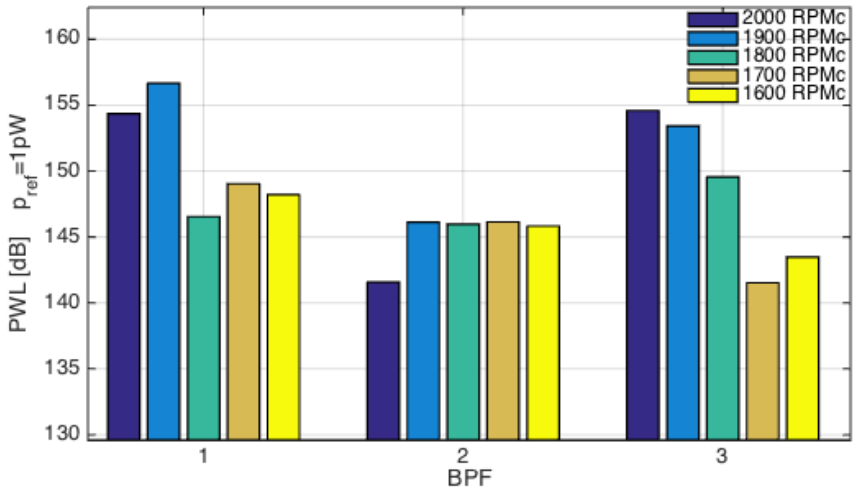

(a) ANCF-NASA Tyler-Sofrin modes power for first to third BPF and five different shaft speeds.

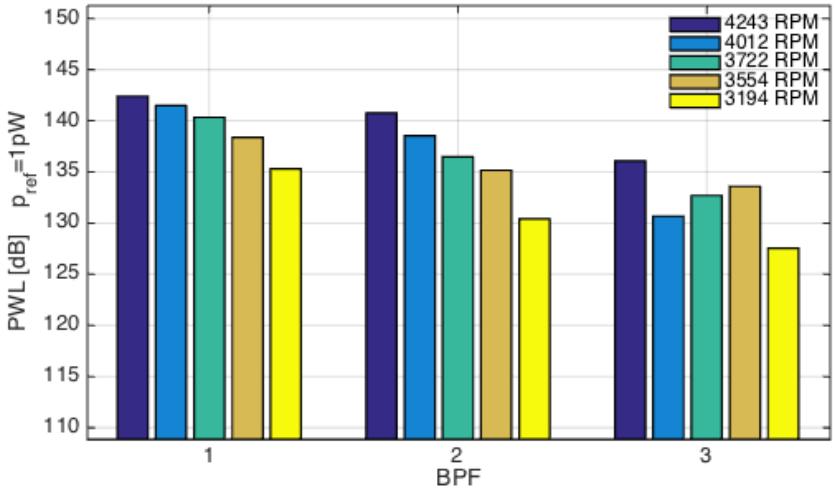

(b) USP fan rig Tyler-Sofrin modes power for first to third BPF and five different shaft speeds.

Figure 40 – Tyler-Sofrin modes power from first to third BPF. For the first BPF, power is computed for $m = +2$. Second BPF $m = +4$ and $m = +6$ for the third BPF.

From second to fourth BPF, their harmonics are easily obtained as $m = +4$ for second BPF, $m = +6$ third BPF and $m = +8$ for the fourth BPF.

Additionally, a possible third order interaction could be detected for some frequencies. This interaction comes from the rotor/stator and struts. That is expressed by $m = nB + kV + sS$, where S is the struts count and s is any integer. For the USP fan rig, 3 struts are supporting the motor enclosure at more or less 1.5 meters downstream from the rotor. Fig. 39 appears to be one example of this interaction. Odd modes like $m = \pm 1, \pm 3, \pm 5$ are possibly related to the interaction with struts. As B and V are even numbers, the only possibility

to obtain odd Tyler-Sofrin modes is by some interaction between rotor/stator and struts. Mode $m = -5$ can be understood as $m = -1 \times 16 + 1 \times 14 - 1 \times 3 = -5$ and the double and opposite signal gives $m = +10$.

One last interesting analysis is shown on Fig. 40. Tyler-Sofrin mode powers are investigated for five different shaft speeds. For each one, the power of all radial modes for a given m mode is computed. For example, for the first BPF, the power plotted corresponds to the sum of all radial modes of mode $m = +2$. For the second BPF all radial modes are summed up for the mode $m = +4$ and same for third BPF and $m = +6$.

Fig. 40(a) corresponding to the ANCF results do not show a clear correlation between shaft speed and modes power. An interesting result is that the second mode $m = +4$ almost does not change with the fan speed. Differently from Fig. 40(b) for the USP fan rig, the mode powers in general decay with decreasing fan speed. Reasons for the difference between rig behaviours would be the different geometries. The ANCF rig has a short duct configuration and as its termination and inlet nuzzle are both close to the fan section, it may cause mode reflections or any other related effect.

5.4 ANCF-NASA BEAMFORMING RESULTS

A compilation of results for the ANCF-NASA is presented in the following sections for rotating and static beamforming. Moreover, a limitation observed in the array for mode detection is also presented.

5.4.1 Static beamforming

Static beamforming was carried out for the ANCF-NASA data. Fan speed was fixed for convenience at 1827 RPM corresponding to a Mach flow of 0.115. The focal plane was placed approximately at the stator plate. Fig. 41 shows the results obtained.

The most interesting fact observed was that for any frequency, a strong source of noise always comes from the left side of the duct and is not distributed in all duct sections as expected for a stator noise (as observed for the USP fan rig in subsection 5.5.1). After discussing these results with engineers from NASA-Glenn, a possible reason is on that side

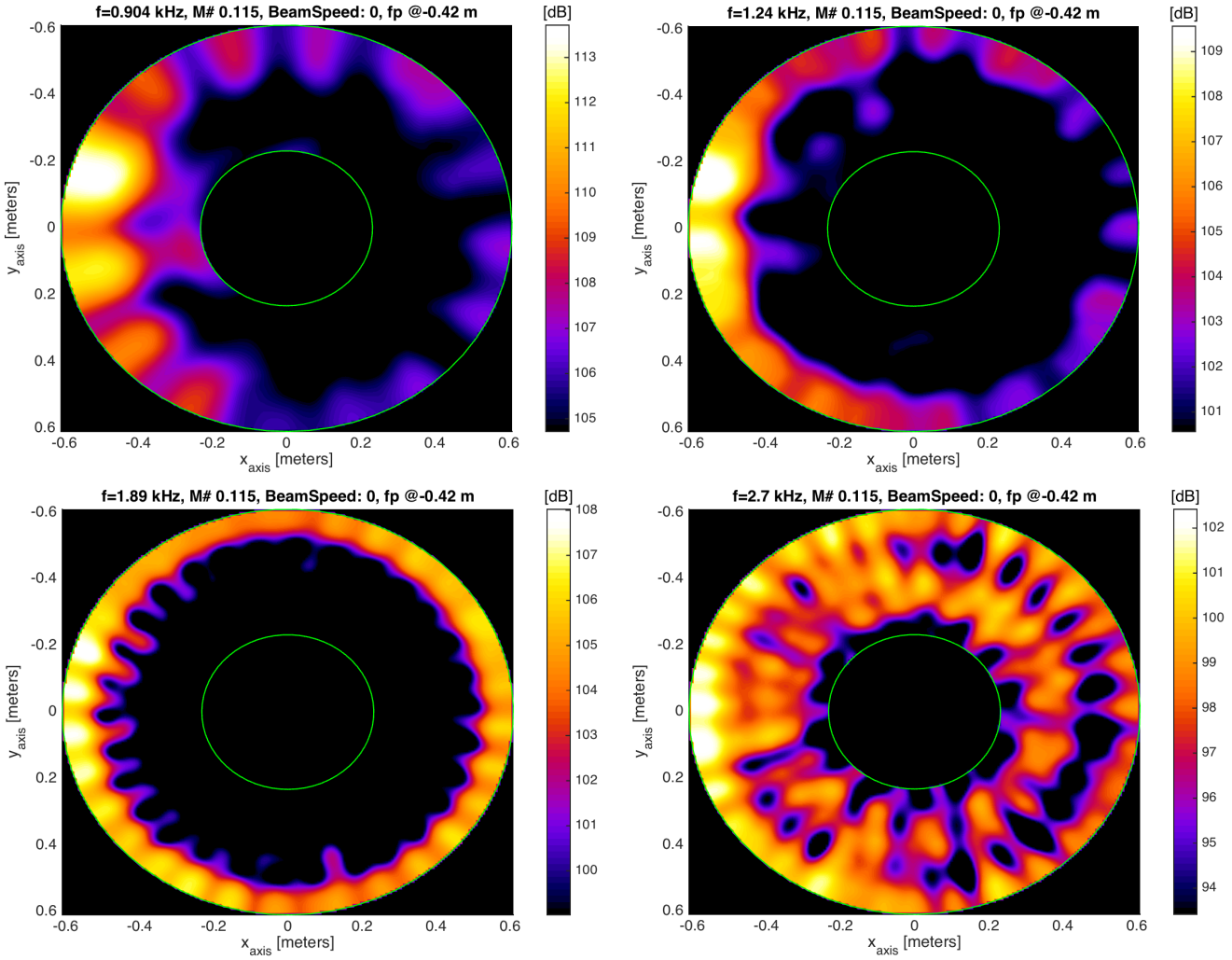

Figure 41 – Static beamforming for the ANCF-NASA. Fan at 1827 RPM and Mach flow 0.115. Focal plane at the stator distance. Four different frequencies are shown.

there is a support pylon and an external stand to support the duct (remember Fig. 22). This stand supports both the duct and the motor that powers up the fan. Perhaps there is some distortion or vibration from that which is responsible for the observations in Fig. 41.

Besides the strong broadband noise source detected at the left-side of the duct, static beamforming makes it much harder to detect coherent noise sources coming from the stator vanes since there are strong rotating sources just in front of it (2, 27). As a result, this means the technique is unable to allow noise coming from the stator vanes to be visualized.

5.4.2 Rotating beamforming

Rotating beamforming maps can be appreciated on Fig. 42. The focal plane was placed at the fan plate. At relatively low frequencies, on the top-left map, it is difficult to

distinguish close sources of noise due to the large array beamwidth. Moreover the acoustic pressure wave propagates more as a one dimensional wave than a three dimensional one.

In all maps we can observe clearly a pattern of 16 noise sources, as expected since this is the same number of blades in the rotor.

The root and mid region of the blades look to be good contributors of noise.

No relevant source of noise coming from the blade tip was observed. This part of the blade is known to produce high frequency noise, yet we did not observe that on the beamforming maps.

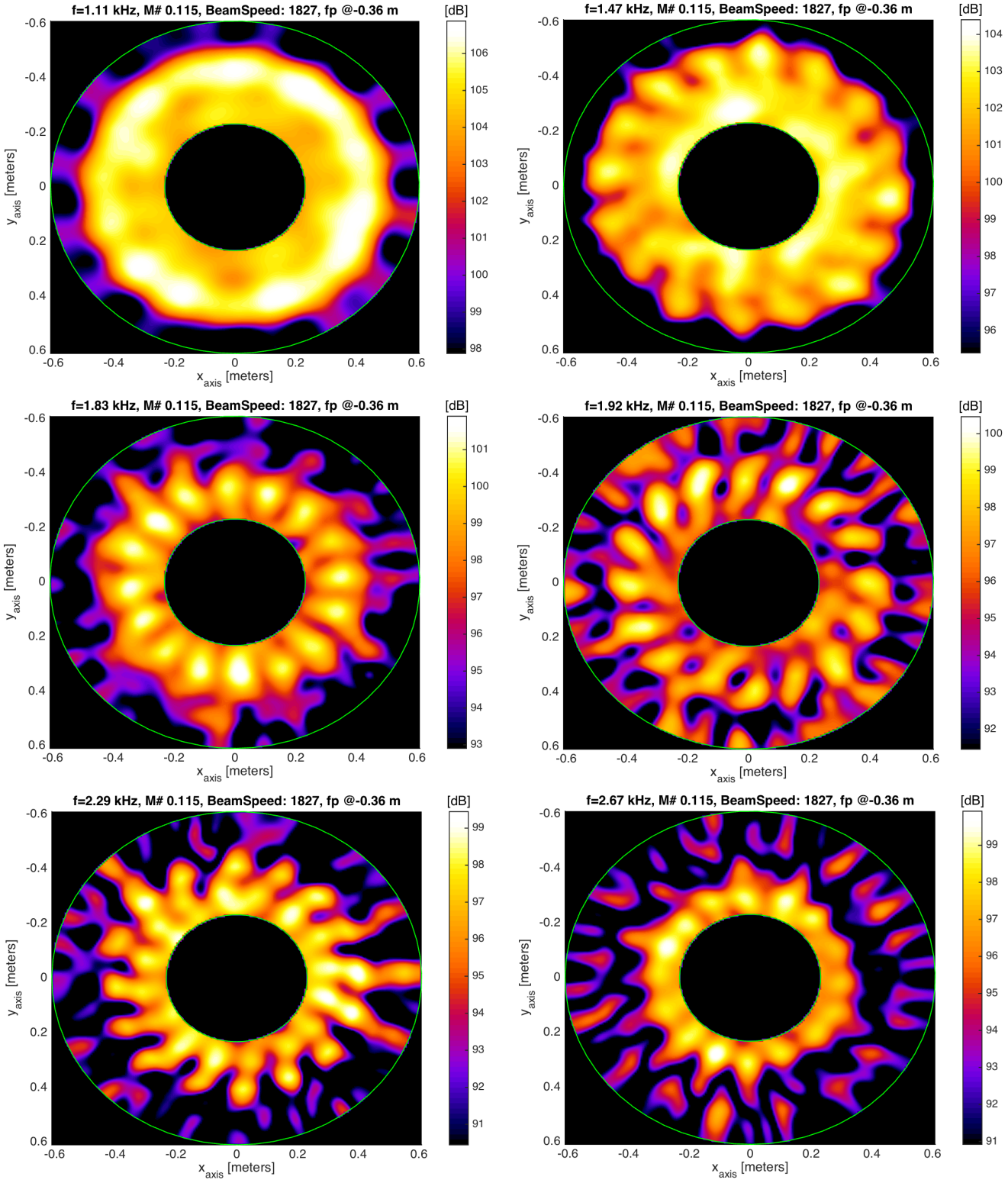

Figure 42 – Rotating beamforming for the ANCF-NASA. Fan at 1827 RPM and Mach flow 0.115. Focal plane at the fan distance. Six different frequencies are shown.

5.4.3 Mode detection: Array limitation

In Section 1.2.1 we introduced the rotating frame reference and the limitation of $m+$ and $m-$ for this new frame of reference. Also the limitation of the array to a maximum detected mode order was discussed in Section 3.1.1. Both theoretical concepts were observed experimentally as shown on Fig. 43.

Modal analysis in this case was performed using many more modes that the array was able to detect. Looking to this modal analysis, based on the asymmetrical shape of cut-on modes $m+$ and $m-$ exposed in Chapter 1 for the rotating frame reference, we believe that only the modes below the green line are cut-on and were rightly detected.

There is a clear difference in the modes below and above the green line, in a way that we suppose that all modes above the green line maybe do not exist. Once the array has a limitation due to the number of microphones per ring.

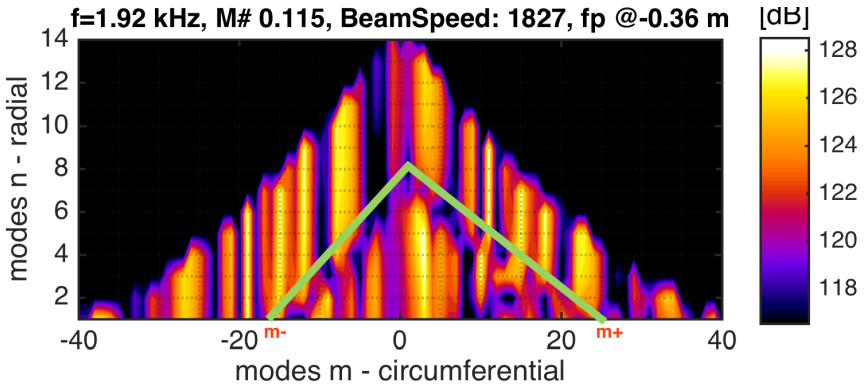

Figure 43 – ANCF mode detection in the rotating frame reference. Shift of $m+$ and $m-$ can be seen besides the array limitation for the maximum mode order detected correctly. Fan at 1827 RPM.

5.5 USP FAN RIG BEAMFORMING RESULTS

A collection of beamforming results for the USP fan rig is presented here. The two green circles correspond to the fan tip (outer ring) and root (inner ring). As discussed in Chapter 4 we used a mesh with 0.6 m diameter, but the fan has only 0.5 m. For this reason the green line is used to help the visualization of the fan region.

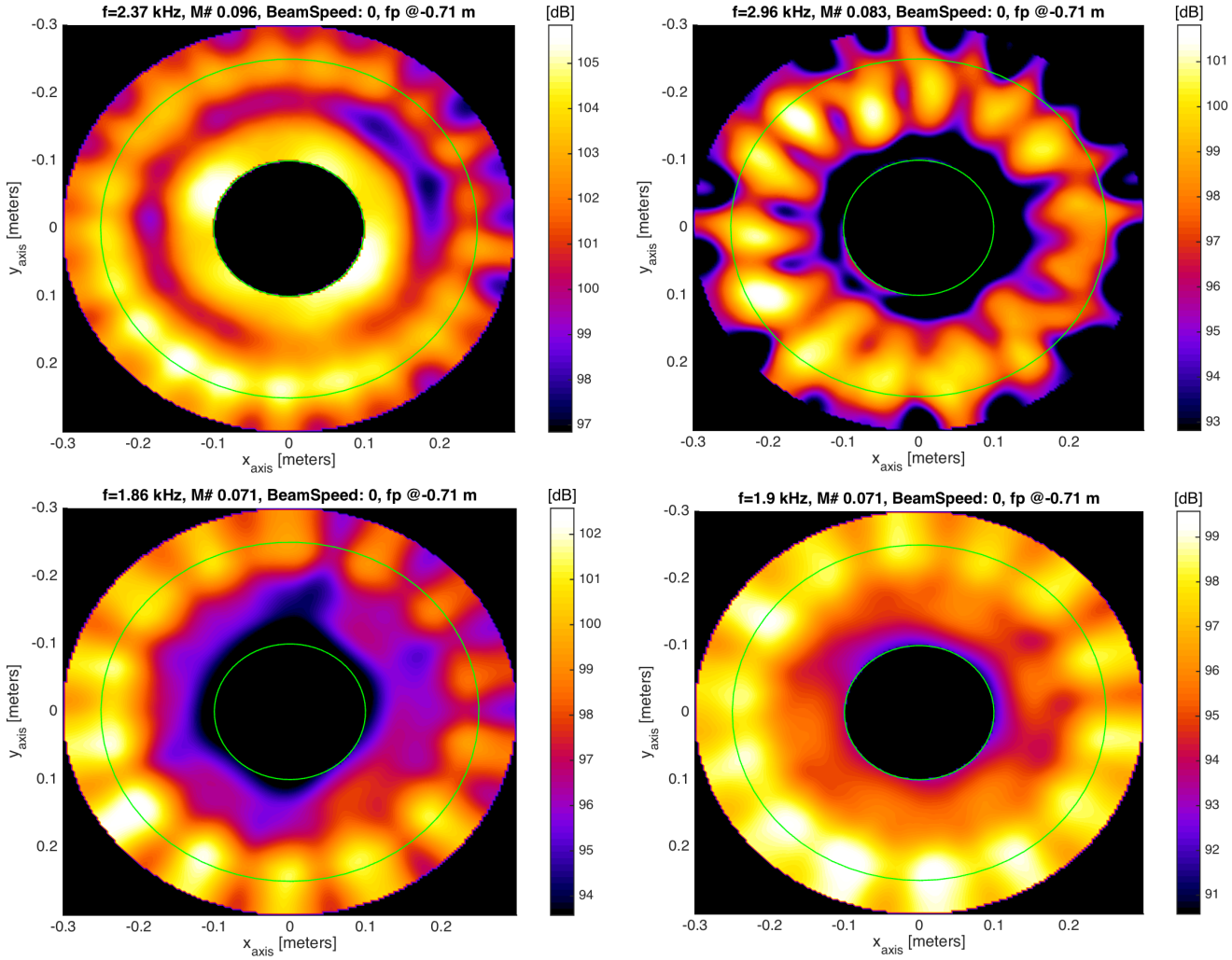

Figure 44 – Static beamforming for the USP fan rig. Left-top map: fan at 4250 RPM. Right-top: fan at 3700 RPM. Bottom maps: fan at 3200 RPM. Focal plane at the rotor distance.

5.5.1 Static beamforming

Results for static beamforming can be seen on Fig. 44. These are clearer than on Fig. 41. For the USP fan rig, it is possible to see a pattern of 14 noise sources, the same count of stator vanes. In bottom maps we can see a strong excited mode shape near the duct wall, i.e., instead of seeing some point noise sources, we see a two-dimensional plane wave due to one strong mode generated at this frequency, similar to those exposed in Fig. 36. In the top-left map the smeared noise from the blades' root and tip is visible.

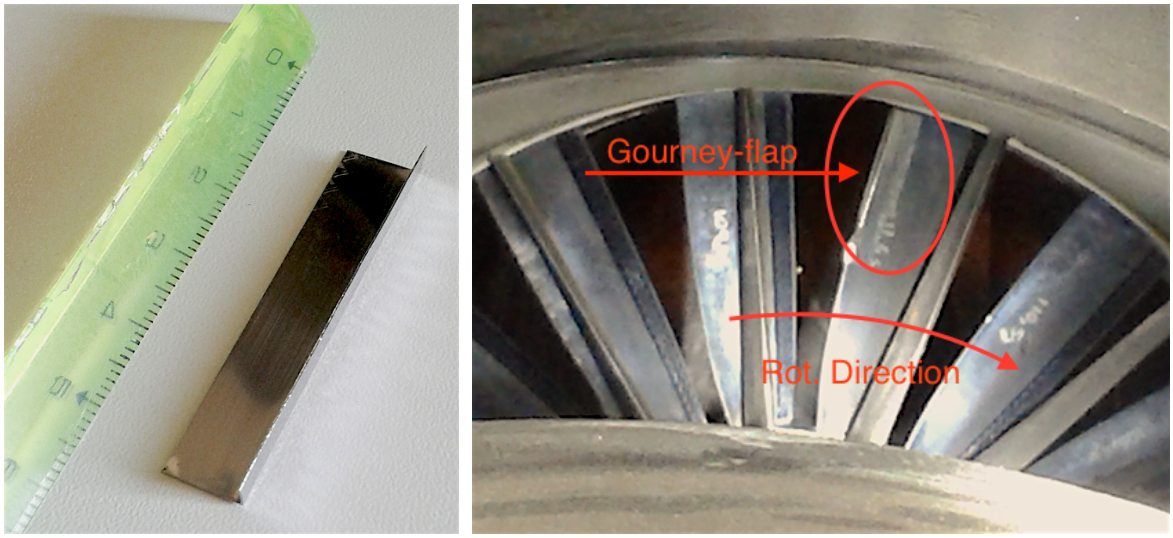

(a) Small L-profile used as a Gurney-flap (b) Rotor's backside view: blade with the Gourney-flap installed on

Figure 45 – Device used to increase the noise produced by one single blade.

5.5.2 Rotating beamforming: Gurney-flap

Aiming to validate the rotating beamforming technique, a small device about 50mm by 3mm was attached on the trailing-edge of one single blade, as seen in Fig. 45. This device works somehow like a Gurney-flap (31), significantly changing blade aerodynamic behavior and hopefully making the blade noisier.

A comparative result for power spectral density (PSD) is presented in Fig. 46, obtained using microphones in the wall-mounted duct-array.

Furthermore, rotating beamforming results is portrayed in Fig. 47 where the left-side shows the baseline results for three different frequencies. Right-side displays the rotating beamforming map for same frequencies, but with the Gurney-flap attached to one blade. It is possible to see that one blade is about 10 dB noisier.

The results of Fig. 47 are coherent with the PSD seen in Fig. 46. The gurney-flap changes the spectra more significantly in the frequency range from the second to the fourth BPF. The larger differences observed were just at those frequencies close to the third BPF (about 2.7 kHz).

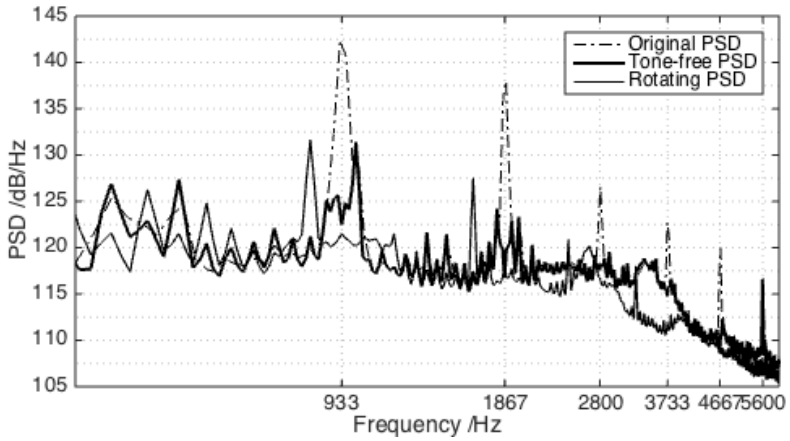

(a) PSD for the baseline case. 3 different plots are shown: Auto-spectra raw; BPF's tone removed; rotating spectra. Fan at 3500 RPM.

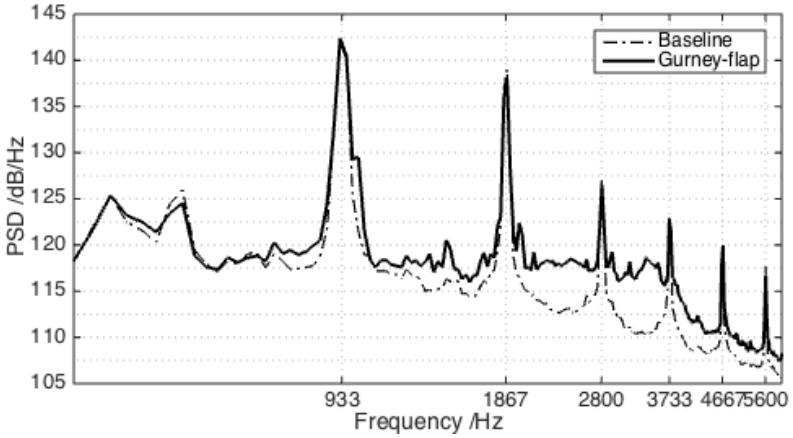

(b) Comparison between PSD: baseline and gurney-flap installed. Fan at 3500 RPM.

Figure 46 – USP fan rig results for power spectra with a gurney flap installed. Fan at 3500 RPM.

5.5.3 Rotating beamforming: Baseline

Fig. 48 portrays six maps for different frequencies. Rotating beamforming was carried out as triggered by the fan speed at 3500 RPM and the focal plane placed at the fan plate. For relative low frequencies, maps on top, we can not distinguish the noise sources from each single blade. However, when frequency increases we can clearly distinguish it, as in mid and bottom maps. On mid maps we observe noise from the blades' root and from the mid span. In higher frequencies only noise from blades' mid span is pronounced.

Even with the approximation equations, i.e., we do not take into account the duct contraction from 0.6 to 0.5 m, we could observe coherent results for beamforming. The noise always come from the fan region (between two green circles) and this is coherent.

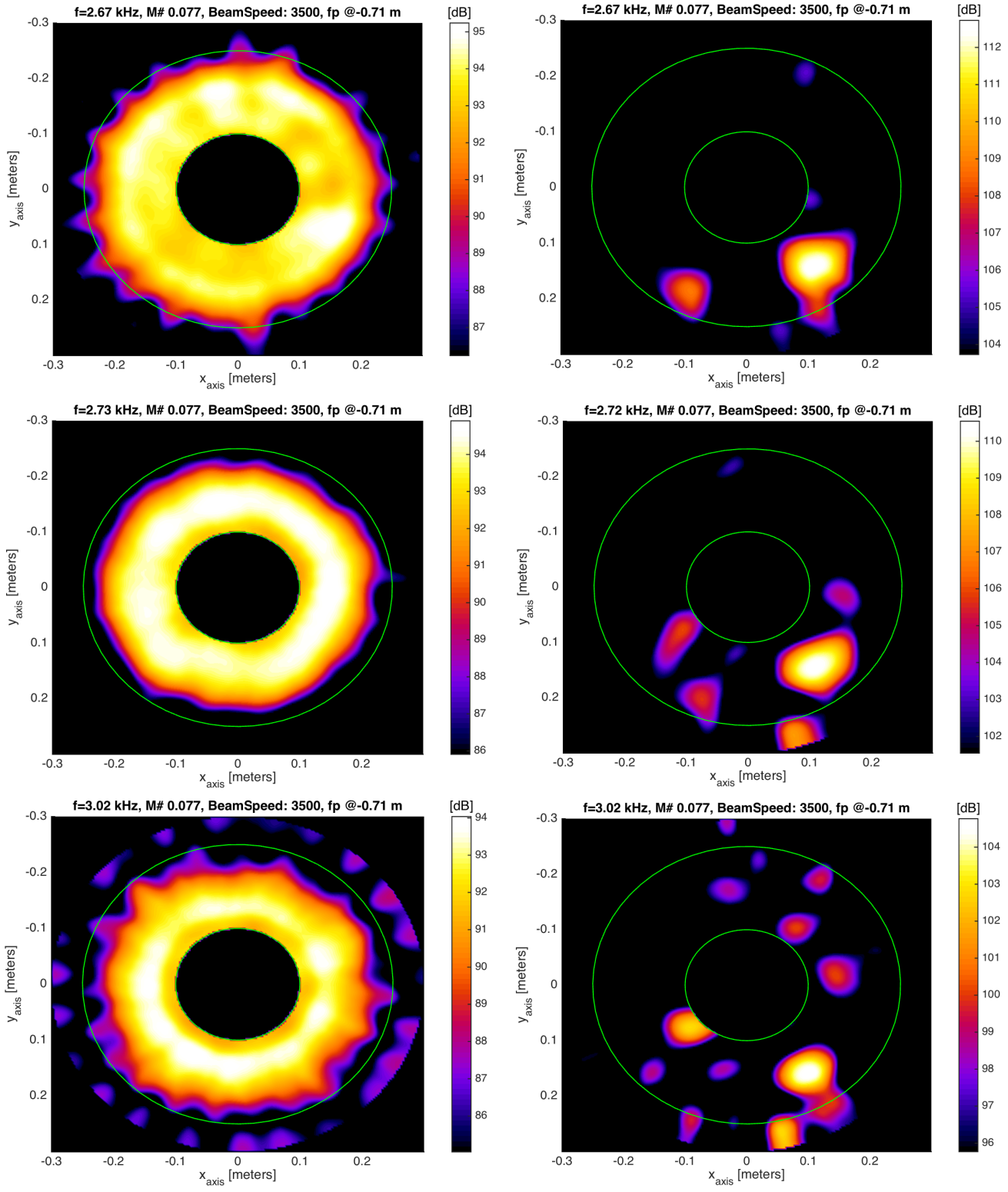

Figure 47 – Conventional Rotating Beamforming results for: (left) Baseline configuration. (right) One blade's trailing-edge modified with a gurney-flap. Fan speed: 3500 RPM

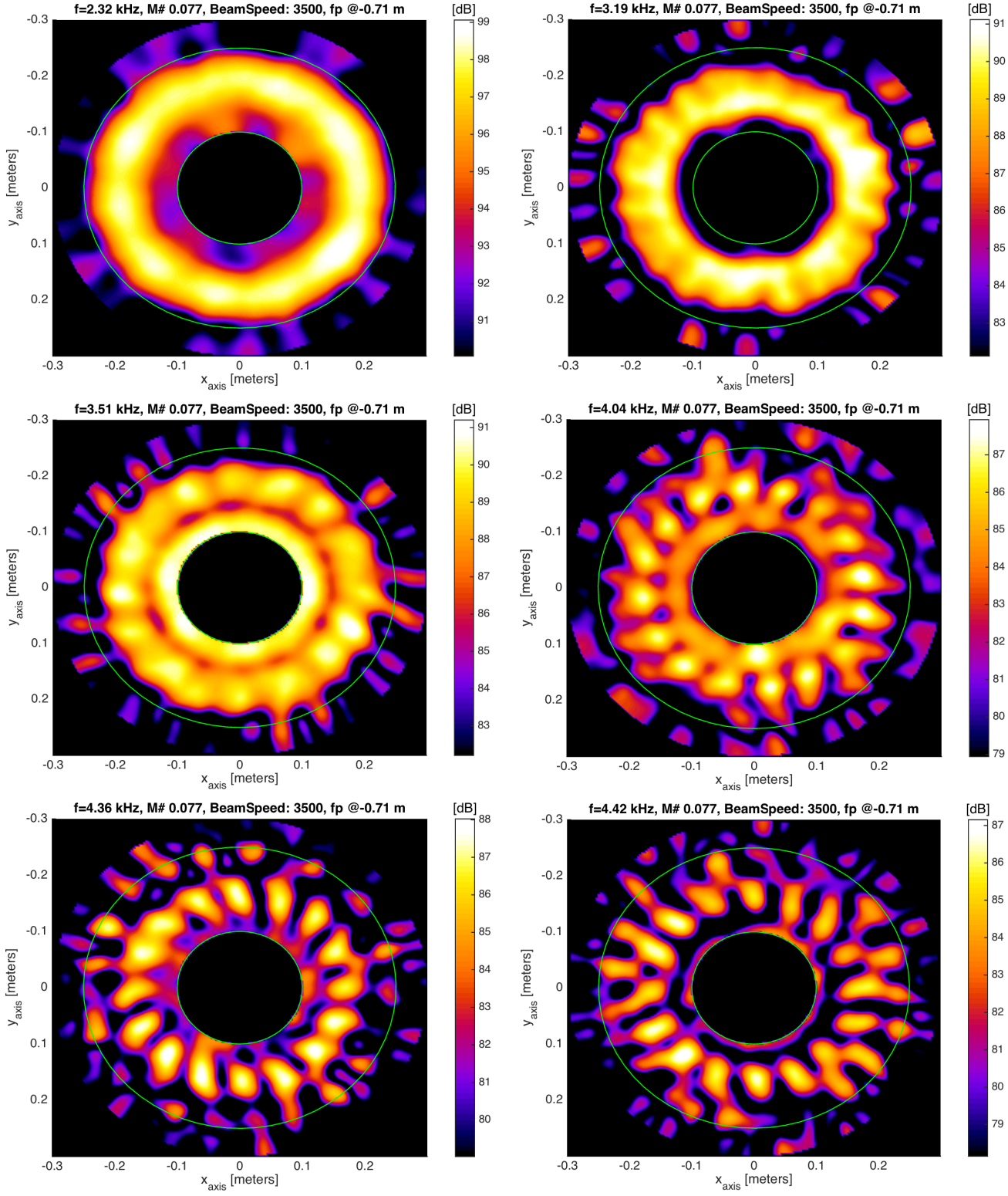

Figure 48 – Rotating beamforming for the USP fan rig. Fan at 3500 RPM and Mach flow 0.077. Focal plane at the fan distance. Six different frequencies are shown.

6 DISCUSSION AND CONCLUSIONS

The present work shows that our in-house developed software for fan noise analysis is a reliable tool. Different sort of analysis were performed and managed to characterize two different fan rigs test facilities.

Fan power spectral density was measured for two different fan rigs test bed. The shape of fan noise was estimated together with theoretically consistent BPF.

An efficient tone removal technique was applied and delivered good results for both rigs. We observed that the broader tones from the USP fan rig do not disappear when the technique is applied, producing a valley that appears at the location of the original tone, revealing that they were not pure tones, i.e., they possibly contain some mixed/modulated nearby frequencies. We suspect that this may be due to the high level of turbulence ingested by the fan, as the rig does not possess an ICD installed as the ANCF-NASA fan rig does.

Results for rotating PSD were also portrayed. We could observe that the shape follows approximately its equivalent static PSD. We found out that tones in the rotating spectra at frequencies just below the BPF for the static spectra, are in fact, BPF tones in the rotating frame, shifted by the change of the frame of reference. The rotating spectra for the ANCF rig was 3dB down in comparison to the static ones. This was not observed in the USP fan rig PSD, which has more or less the same energy level.

The mode detection code showed relevant results for the data acquired from the synthetic mode generator at ANCF-NASA Glenn. The powerful modes observed match the predicted ones. Moreover, Tyler-Sofrin modes were detected for both rigs from the first to the fourth order for rotor and stator interaction. For the USP fan rig, a possible third order interaction with three struts was also observed regarding the odd modes detected. Finally, the pattern of Tyler-Sofrin mode power was plotted for different shaft speeds. The rigs showed a completely different behavior. We do not know the exact reason for that, but a suspect would be the short duct configuration of the ANCF rig. The USP fan rig had mode power decrease at lower fan speeds. This is expected since the total noise power is proportional to fan speed.

Static beamforming using the ANCF-NASA data exposed a peculiar source of broadband noise coming from the left side of the duct, when looking towards the inlet. This was observed at all frequencies. The most probable reason is the presence of the pylon that supports the duct and the electrical motor. The vibration of the rotating system (i.e., motor, shaft, bearings, belt, etc.) is transmitted by the pylon to the duct, and that vibration is probably being detected by the static beamforming procedure. For the USP fan rig setup, static beamforming was able to detect coherent sources related to the stator vanes. Some results exhibit a pattern of 14 noise sources, mirroring the vane count. Smeared noise is also seen due to the fan spinning in front of the stator plate. Many times we observed that static beamforming reveals one dimensional waves, i.e., what we see is, in fact, a mode shape in the image instead of discrete noise sources.

Rotating beamforming, the most important technique in terms of noise analysis for fan noise, showed interesting results. For both rigs noise coming from the blades and a pattern of 16 noise sources are seen in the maps. For relative low frequencies it is difficult to distinguish close sources because of the array's large beamwidth. On the other hand, when the frequency increases, the later pattern clearly emerges. For the USP fan rig, even using an approximation for the steering vector that neither takes into account the duct contraction nor the increasing of the Mach number, the results obtained are in agreement with those observed in the references. When the gurney flap was attached to one blade, we observed it as an evidently much noisier blade. The side-by-side comparison in frequency to the baseline highlights this conclusion.

Finally, we can conclude that with the developed software, despite its limitations and approximations, we obtained coherent results in terms of beamforming and mode detection, just as expected due to the references used here. Furthermore, techniques for signal processing led to interesting results in terms of power spectral densities when comparing both rigs, BPF tones, spectra shape, and rotating reference frame results.

BIBLIOGRAPHY

1 NALLASAMY, M.; SUTLIFF, D. L.; HEIDELBERG, L. J. Propagation of spinning acoustic modes in turbofan exhaust ducts. *JOURNAL OF PROPULSION AND POWER*, v. 16, n. 5, p. 736–743, September-October 2000. Cited on page 13.

2 LOWIS, C. R. *In-duct measurement techniques for the characterisation of broadband aeroengine noise*. Tese (Doutorado) — University of Southampton, Southampton, England, 2007. Cited 7 times on pages 13, 17, 20, 27, 36, 43, and 66.

3 DOUGHERTY, R. P.; MENDONZA, J. M. Nacelle in-duct beamforming using modal steering vectors. In: *14th AIAA/CEAS Aeroacoustics Conference (29th AIAA Aeroacoustics Conference)*. American Institute of Aeronautics and Astronautics, 2008. Disponível em: <http://dx.doi.org/10.2514/6.2008-2812>. Cited 3 times on pages 13, 30, and 62.

4 DOUGHERTY, R. P.; WALKER, B. E. Virtual rotating microphone imaging of broadband fan noise. In: *15th AIAA/CEAS Aeroacoustics Conference (30th AIAA Aeroacoustics Conference)*. American Institute of Aeronautics and Astronautics, 2009. Disponível em: <http://dx.doi.org/10.2514/6.2009-3121>. Cited 6 times on pages 13, 17, 20, 37, 42, and 43.

5 DOUGHERTY, R. P.; WALKER, B. E.; SUTLIFF, D. L. Locating and quantifying broadband fan sources using in-duct microphones. In: *16th AIAA/CEAS Aeroacoustics Conference*. American Institute of Aeronautics and Astronautics, 2010. Disponível em: <http://dx.doi.org/10.2514/6.2010-3736>. Cited 3 times on pages 13, 30, and 45.

6 SIJTSMA, P. Feasibility of in-duct beamforming. In: *13th AIAA/CEAS Aeroacoustics Conference (28th AIAA Aeroacoustics Conference)*. [S.l.]: American Institute of Aeronautics and Astronautics, 2007. Cited 3 times on pages 14, 42, and 43.

7 SUTLIFF, D. L. Rotating rake turbofan duct mode measurement system. In: *NOISE-CON*. Institute of Noise Control Engineering, 2005. Disponível em: <http://dx.doi.org/10.1121/1.4779000>. Cited on page 14.

8 SARRADJ, E. Three-dimensional acoustic source mapping with different beamforming steering vector formulations. *Advances in Acoustics and Vibration*, v. 2012, n. ID 292695, p. 12, 2012. Disponível em: <http://dx.doi.org/10.1155/2012/292695>. Cited 2 times on pages 17 and 20.

9 ALONSO, J. S.; BURDISSO, R. A. Eigenvalue solution for the convected wave equation in a circular soft wall duct. *Journal of Sound and Vibration*, v. 315, n. 4-5, p. 1003–1015, September 2008. Cited on page 17.

10 KIM, Y.; NELSON, P. A. Estimation of acoustic source strength within a cylindrical duct by inverse methods. *Journal of Sound and Vibration 275 (2004) 391-413*, 2004. Cited on page 17.

11 RIENSTRA, S.; HIRSCHBERG, A. *An Introduction to Acoustics*. [S.l.]: Eindhoven University of Technology, 2014. Cited on page 17.

12 BEATTIE, C. L. Table of first 700 zeros of Bessel functions - $J_l(x)$ and $J'l(x)$. *Bell System Technical Journal*, v. 37, n. 3, p. 689–697, May 1958. Cited on page 19.

13 PERCIVAL, D. B.; WALDEN, A. T. *Spectral Analysis for Physical Applications*. [S.l.]: Cambridge University Press, 1993. Cited 3 times on pages 25, 38, and 39.

14 KAY, S. M. *Modern Spectral Estimation: Theory & Application*. [S.l.]: Englewood Cliffs, N.J. : Prentice Hall, 1987. Cited 4 times on pages 25, 28, 38, and 39.

15 STOICA, P.; MOSES, R. L. *Introduction to spectral analysis*. [S.l.]: Prentice Hall, 1997. Cited 2 times on pages 25 and 38.

16 SIJTSMA, P. Clean based on spatial source coherence. In: AIAA. *13th AIAA/CEAS Aeroacoustics Conference (28th AIAA Aeroacoustics Conference)*. [S.l.], 2007. Cited on page 27.

17 PANNERT, W.; MAIER, C. Rotating beamforming - motion-compensation in the frequency domain and application of high-resolution beamforming. *Journal of Sound and Vibration*, v. 333, n. 7, p. 1899–1912, 2014. Cited on page 36.

18 HEROLD, G.; SARRADJ, E. Microphone array method for the characterization of rotating sound sources in axial fans. *Noise Control Engineering Journal*, v. 63, n. 6, p. 546–551, 2015. Cited on page 36.

19 MUELLER, T. J. *Aeroacoustic Measurements*. [S.l.]: Springer, 2001. Cited 2 times on pages 38 and 39.

20 TRöBS, M.; HEINZEL, G. Improved spectrum estimation from digitized time series on a logarithmic frequency axis. *Measurement 39*, v. 42, n. 2, p. 120–129, 2006. Disponível em: <dx.doi.org/10.1016/j.measurement.2005.10.010>. Cited on page 39.

21 MOREAU, A. Ranking of fan broadband noise sources based on an experimental parametric study. *15th AIAA/CEAS-2009-3222 Aeroacoustics Conference, Florida*, 2009. Cited on page 42.

22 LOEW, R. A. et al. The advanced noise control fan. *NASA/TM-2006-214368, also AIAA-2006-3150*, 2006. Cited 2 times on pages 42 and 47.

23 FONSECA, W. et al. A different approach to archimedean spiral equation in the development of a high frequency array. *SAE International*, 2010. Disponível em: <http://papers.sae.org/2010-36-0541/>. Cited on page 45.

24 LAUCHLE, G. C. *Centrifugal and axial fan noise prediction and control*. [S.l.]: John Wiley & Sons, Inc., 2007. Cited on page 47.

25 BARLOW, J. B.; RAE, W. H.; POPE, A. *Low-speed wind tunnel testing*. [S.l.]: New York: Wiley-Interscience, 1999. Cited on page 47.

26 SUTLIFF, D. L. A mode propagation database suitable for code validation utilizing the nasa glenn advanced noise control fan and artificial sources. In: *52nd Aerospace Sciences Meeting*. [S.l.: s.n.], 2014. Cited 2 times on pages 47 and 61.

27 CALDAS, L. C. et al. In-duct beamforming noise source estimation and mode detection at the university of são paulo fan rig. In: *21st AIAA/CEAS Aeroacoustics Conference*. American Institute of Aeronautics and Astronautics, 2015. Disponível em: <http://dx.doi.org/10.2514/6.2015-2233>. Cited 3 times on pages 60, 61, and 66.

28 TYLER, J. M.; SOFRIN, T. G. Axial flow compressor noise studies. *Transactions of the society of automotive engineers*, v. 70, p. 309–32, 1962. Cited 2 times on pages 60 and 62.

29 ENGHARDT, L.; MOREAU, A.; KAUSCHE, P. Active control of fan tones by means of trailing edge blowing. In: *21st AIAA/CEAS Aeroacoustics Conference*. American Institute of Aeronautics and Astronautics, 2015. Disponível em: <http://dx.doi.org/10.2514/6.2015-2828>. Cited on page 62.

30 SUTLIFF, D. L. Broadband noise reduction of a low-speed fan noise using trailing edge blowing. In: *NASA/TM-2005-213814, also AIAA–2005–3028*. [S.l.: s.n.], 2005. Cited on page 62.

31 WANG, J. J.; LI, Y. C.; CHOI, K. S. Gurney flap - lift enhancement, mechanisms and applications. *Progress in Aerospace Sciences*, v. 44, n. 1, p. 22–47, January 2008. Disponível em: <http://dx.doi.org/10.1016/j.paerosci.2007.10.001>. Cited on page 71.

Annex

ANNEX A – MATLAB EXAMPLE CODES

Matlab codes for spectra estimation and validation. It is necessary the 'Signal Processing' toolbox.

>>welch_estimator.m

```
%% Function for spectra estimation by Welch's method
% Developed by Luiz A. Baccala, Flavio Caduda and Luciano Caldas, all from
% Escola Politecnica - Poli-USP, with cooperation of Carlos Pagani and Felipe
% Amaral from Escola de Engenharia de Sao Carlos - EESC-USP.
%
% Cross-spectra matrix are estimated by Welch's method with 50% overlap and
% the window energy loss are compasated by a factor of 1/sum(Wi.^2) where
% Wi are the elements of the window [1]. Then, the spectra becomes:
% Sxy = fft(x)*conj(fft(y))/sum(Wi.^2)
%
% Code was tested with a known- spectra signal from a white noise filtered
% by a filter. The variance (power) of the signal checks with the integral
% of the PSD estimated.
%
% INPUT:
% -- signals: matrix of signals to perform the spectra estimatino. Size is
% [Samples x number of sensors];
% -- fs: samplerate in Hertz;
% -- window: data taper desired. Must be a vector. For best performance it
% should be a power of 2. For general applications do: window=hanning(1024);
%
% OUTPUT:
% -- CSM: Cross Spectral Matrix: Unilateral (0:fs/2) spectra. Welch's
% method is used with 50% overlap. Matrix size: sensors x sensors x
% windowsize/2
% -- frequencies: vector with all frequencies corresponding to each layer
% (3rd layer in depth) of CSM.
%
% LAST REVISION: September - 11 - 2015
% [1] Trobs,M.; Heinzel,G. "Improved spectrum estimation from digitized
% time series on a logarithmic frequency axis"
% doi:10.1016/j.measurement.2005.10.010

function [CSM,frequencies] = welch_estimator(signals,fs,window)

if size(signals,2) > size(signals,1)
    signals = signals.';
end
window = window(:);
sensors = size(signals,2);
windowsize = length(window);
frequencies = (0:(windowsize/2-1))*fs/windowsize;
block_samples = windowsize; %must be even, best if 2^n

signal_samples = size(signals,1);
number_of_signals = size(signals,2);
back_shift = block_samples./2;
number_of_blocks = floor((2*signal_samples)./block_samples) -1;

data_taper = window;
data_taper = repmat(data_taper,1,number_of_signals);

% Data segmentation into blocks of size block_samples:
S = zeros(block_samples/2,number_of_signals.^2);
for a = 1:number_of_blocks
    % Retrieve current data block
    Data_Block = signals((a-1)*back_shift+1:block_samples +(a-1)*back_shift,:);
```

```
    Data_Block = Data_Block - repmat(mean(Data_Block),block_samples,1);
    Data_Block = Data_Block.*data_taper;        %Taper it

    Data_Block = fft(Data_Block);    %FFT it,
    % bilateral DFT
    Data_Block = Data_Block(1:block_samples/2,:);

    %All spectral combinations:
    P = zeros(block_samples/2,number_of_signals.^2);
    c = 1;
    for aa = 1:size(Data_Block,2)
        for b = aa:size(Data_Block,2)
%                 P(:,c) = Data_Block(:,b).*conj(Data_Block(:,aa)); % THIS
%                 IS FOR WIND TUNNEL EESC-USP BEAMFORMING CODE
              P(:,c) = Data_Block(:,aa).*conj(Data_Block(:,b)); % THIS
%                 IS FOR FAN RIG BEAMFORMING CODE
            c = c+1;
        end
    end
    % Sum the spectrums up ...
    S = S + P;
end

S = S*2/(sum(window.^2)*number_of_blocks); % Average them out
Sf = zeros(sensors,sensors,size(S,1));
c=1;
for a = 1:sensors
    for b = a:sensors
        Sf(a,b,:) = S(:,c);
        c = c+1;
    end
end
clear S
CSM = Sf;
for i = 1:size(CSM,3)
    CSM(:,:,i) = CSM(:,:,i) + CSM(:,:,i)' - eye(sensors).*CSM(:,:,i);
end
end
```

Code to test the Welch estimator algorithm

>> test_spectra.m

```
clear all; clc; close all
% model parameters for test
r = 0.99;           % Radius of the first pole
kk = 1:5;
rr = r.^kk;         % all poles' radius
thetha = pi/7;      % First pole angle
thethar = thetha.*kk;   % all poles' angle
rN = 14;
rM = 4;
Burnin = 10000;
x = randn(1,Burnin+2^(rN+1)); % white noise
% para gerar espectro te?rico do sinal de teste
xa = 1;
for i=1:5
    % 'xa' will have the coefficients for the theoretical spectra
    xa = conv([1 -2*rr(i)*cos(thethar(i)) rr(i)^2],xa);
    x = filter(1,[1 -2*rr(i)*cos(thethar(i)) rr(i)^2],x); % filter the signal
    % to then generate 5 tonal peaks
end
% burn the transient
x = x(Burnin+1:end);
%%
linewidth = 1.3;
x = x(:);
disp(['signal variance: ' num2str(var(x))])
```

```
figure, hold on;
[ft,w]=freqz(1,xa,1024);
plot(w*.5/pi,20*log10(abs(ft)),'r.','LineWidth',linewidth)
wind = [1024 512 256 128];
for i=1:length(wind)
    [spec,f]=welch_estimator(x,1,hann(wind(i)));
    plot(f,10*log10(abs(reshape(spec/2,length(f),1))),'LineWidth',linewidth)
    disp(['PSD integral w/ L=' num2str(wind(i)) ': ' num2str(sum(spec)*f(2))])
end

legend(    'theoretical spec',...
    ['Window ' num2str(wind(1))],...
    ['Window ' num2str(wind(2))],...
    ['Window ' num2str(wind(3))],...
    ['Window ' num2str(wind(4))])
xlabel('Normalized frequency'); ylabel('PSD [dB]');
title('Power spectra test');
grid
set(gca, 'FontSize', 13)
```

Duct beamforming code. It is necessary other codes not shown here. This is only the backbone to show the formulation used, for example the steering vector formulation.

>> duct_beamforming.m

```
function [CBF_output] = duct_beamforming(CBF_parameters)

%% %%%%%%%%%%%%%% Beamforming code for IN-DUCT Analysis %%%%%%%%%%%%%%%%%
% Developed by Luciano Caldas (Master student) and Luiz A. Baccala
% (advisor) for FAN-Noise analysis.
% Escola Politecnica and EESC - USP.
%
% Last revision: 2015-Dec

%%%%%%%%%%%%%%%%%%%%%%%%%%%%%%%%%%%%%%%%%%%%%%%%%%%%%%%%%%%%%%%%%%%%%%%%%%%
%
% ---------- MECHANICAL PARAMETERS ----------------------------------------
% a:             [m]     Duct radius
% z_s:           [m]     Focal plane distance
% r_s0:          [m]     Hub radius
% rotor_RPM:     [RPM]   FAN shaft speed
% W:             [rad/s] FAN shaft speed

% ---------- ELECTRICAL PARAMETERS ----------------------------------------
% windowsize:    []      Window size used for the spectra estimation
% samplerate:    [Hz]    Sample rate used in the data acquisition
% sensors:       []      Number of sensors
% frequency:     [Hz]    Frequency for beamforming sweep
% freq:          []      CSM layer to the corresponding frequency
% f:             [Hz]    Nearest frequency due the windowsize/samplerate
% CSM:           []      Cross-spectral matrix

% ---------- AERO/ACOUSTIC PARAMETERS -------------------------------------
% M:             []      Mach number
% c:             [m/s]   Speed of sound
% k:             [rad/m] Wave vector, corrected for the mode/shaft speed
% p_ref:         [Pa]    Reference pressure, 20uPa
% d_range:       [dB]    Dynamic range to display in the beamforming map
% total_modes:   []      Total number of modes
% sig:           []      Stationary points of Jm(x) -> zeros of J'm(x)
% mode:          []      'm' mode corresponding to each value in 'sig'

% ---------- MESH DEFINITIONS ---------------------------------------------
% n_theta        []      Number of points in the mesh: theta direction
% n_rs           []      Number of points in the mesh: radius direction
% span_rs        [m]     Span of the mesh in radius direction
```

```
% span_theta    [rad]   Span of the mesh in theta direction
% r_a           [m]     Maximum radius of the mesh (region of interest)

% ---------- BEAMFORMING PARAMETERS ---------------------------------------
% g:            []      Steering vector
% g_targ:       []      Steering vector in a target reference for PSF
% B:            [dB/m]  Beamforming map
% psf:          []      Point Spread Function (PSF) map
%
% 'psi_r; psi_rs; gamma; exp1; exp2' was the same as reference text: Lowis
% 2007 thesis.
%
%%%%%%%%%%%%%%%%%%%%%%%%%%%%%%%%%%%%%%%%%%%%%%%%%%%%%%%%%%%%%%%%%%%%%%%%%%%

a           = CBF_parameters.DuctRadius;          % [m]   Duct radius
N           = CBF_parameters.MeshSize;
r_fan       = CBF_parameters.FanRadius;               % [m]   Fan radius
Z_S         = CBF_parameters.FocalPlane;                    % [m]   Focal plane
r_s0        = CBF_parameters.RubRadius;
run         = CBF_parameters.RunNumber;
layer       = CBF_parameters.EvaluatingLayers; % Frequencies layers to evaluate the beamforming
temp        = CBF_parameters.Temperature;                      % [oC]  Temperature in celcius degrees
frpm        = CBF_parameters.BeamSpeed;                    % [RPM] Rotating beamforming speed
M           = CBF_parameters.MachNumber;
frequencies = CBF_parameters.Frequencies;
fs          = CBF_parameters.SampleRate;
Sf_rotating = CBF_parameters.RotatingCrossSpectralMatrix;
Sf_static   = CBF_parameters.StaticCrossSpectralMatrix;
mics_coordinates = CBF_parameters.MicsCoordinates;
d_range     = CBF_parameters.DynamicRange;
mode_detection = CBF_parameters.ModeDetection;

%% Mechanical parameters
sensors     =       length(mics_coordinates);
c           =       sqrt(1.4*287.0586*(273.15 + temp));     % [m/s] sound speed
W           =       frpm*2*pi/60;  % [rad/s] FAN speed

%%
disp('Evaluating Conventional Duct-Beamforming');
disp(['Mach Flow: ' num2str(M)]);
disp(['Beam Speed: ' num2str(frpm) 'RPM']);
disp(['Number of Microphones: ' num2str(sensors)]);
disp(['Sound of speed: ' num2str(c) 'm/s']);

%% Mesh definitions
r_a = a;
% N = 200;
x_mesh = linspace(-r_a,r_a,N);
y_mesh = linspace(-r_a,r_a,N);

% sensor position: cilindrical coord:       (X: r,theta,z )
% source mesh position: cilindrical coord:  (?Y: r_s, theta_s, z_s)

disp(['Mesh grid: ' num2str(N) 'x' num2str(N) ' dots']);
disp(['Duct radius: ' num2str(a) 'm']);
disp(['Focal plane distance: ' num2str(Z_S) 'm']);



%% Pre-allocating variables

B = 1e-20*ones(N,N,length(frequencies),length(Z_S));
psf_w = zeros(length(frequencies),1,length(Z_S));
PSF = 1e-20*ones(N,N,length(frequencies),length(Z_S));
time_spent = zeros(length(frequencies),length(Z_S));

Number_of_modes = zeros(length(frequencies),1);
b_modes = 1e-20*ones(400,length(frequencies));
Modes = zeros(400,2,length(frequencies));
```

```
%% Beamforming!
for dm_zs = 1:length(Z_S)               % Focal plane loop
    z_s = Z_S(dm_zs);
    cont_freq = 1;
    for dm_freq = layer %1:length(frequencies) % Frequencies loop
        tic
        freq = dm_freq;
        f = frequencies(dm_freq);

        %% Selection of modes in cut-on
        sigma_cut_off = 25;
        sigma_MAX = 2*pi*f*a/(c*(1-M^2));
        sigma_MAX = sigma_MAX*(2-sigma_MAX/sigma_cut_off);
        if sigma_MAX > sigma_cut_off %reduced from 90 to 25. m_{max} < 20
            sigma_MAX = sigma_cut_off;
        end
        if sigma_MAX < 12
            sigma_MAX = 12;
        end
        load sigma2
        [sig,I] = sort(sigma2(:));
        max_pos = find(sig <= sigma_MAX);
        sig = sig(1:max_pos(end));
        m_modes = -40:40; m_modes = m_modes(:);
        m_modes = repmat(m_modes,16,1);
        n_modes = 1:16; n_modes = repmat(n_modes,81,1);
        n_modes = n_modes(:);
        n_modes = n_modes(I(max_pos));
        mode = m_modes(I(max_pos));
        total_modes = length(mode);
        Number_of_modes(dm_freq) = total_modes;
        %% Bessel constants
        % psi_r depends only on radius of sensors, not of the mesh point. So, these
        % constants are pre-calculated before the mesh-loop to improve speed.

        k = (2*pi*f +mode(:)*W)./c;
        kappa = sqrt( k.^2 -(1-M^2)*(sig/a).^2 );
        gamma1 = (-M*k -kappa)/(1-M^2);
        gamma2 = (-M*k +kappa)/(1-M^2);
        gamma = gamma1;
        psi_r = besselj(mode(:),sig);
        lambda = (1- (mode.^2)./sig.^2).*(abs(psi_r).^2);
        lambda(1,1) = abs(besselj(0,sig(1)))^2;

%         psi_r = psi_r./(lambda.*kappa);
        psi_r = psi_r./(lambda);

        %% Target for PSF
        % g = zeros(total_modes,sensors); %column vector
        theta_psf = 0;
        r_psf = a/2;
        psi_rs = besselj(mode(:),sig*r_psf/a);
        psi = psi_r.*psi_rs; %.*(2*pi*f +mode(:,1)*W)); %[635x1]

        theta = mics_coordinates(:,2)';
        z = mics_coordinates(:,3)';

        exp1 = exp(1i*mode(:)*(theta-theta_psf));
        exp2 = exp(-1i*gamma*(z-z_s)); % [207x100]

        g = repmat(psi,1,sensors).*exp1.*exp2;
        % g2 = g*1i/(4*pi);
        % g_targ = g2.'/norm(g2);
        g_targ = sum(g,1);
    %     w_targ = g_targ/norm(g_targ); % [100x1]

        %% Duct Beamformer
        if frpm == 0
            CSM = Sf_static(:,:,freq);
        else
```

```
            CSM = Sf_rotating(:,:,freq);
        end

        A = ones(sensors,sensors) - eye(sensors);
        r = mics_coordinates(1,1);     % radius of sensor

        psf = ones(N,N)*1e-20;
        B2 = ones(total_modes,total_modes);
        B_modes = ones(N,N,total_modes)*1e-20;

        g = zeros(total_modes,sensors); % Matrix with modes in rows for each microphone
        % in columns.
        % >> arrayfun; matlabpool('open')
        parfor x_grid = 1:N
            for y_grid = 1:N

                r_s = sqrt(y_mesh(y_grid)^2 + x_mesh(x_grid)^2);
                theta_s = asin(y_mesh(y_grid)/r_s);
                if x_mesh(x_grid) < 0
                    theta_s = -(pi+theta_s);
                end

%                 if (r_s >r_a || r_s < r_s0)
                if (r_s >a)

                else

                    psi_rs = besselj(mode(:),sig*r_s/a);  % Same notation as Lowis thesis

                    psi = psi_r.*psi_rs; %.*(2*pi*f +mode(:,1)*W)); %[635x1]
                    exp1 = exp(1i*mode(:)*(theta-theta_s)); % [635x64] = [ modes x sensors]

                    g = repmat(psi,1,sensors).*exp1.*exp2;

                    if mode_detection == 'y'
                        B2 = g*(CSM.*A)*g'./(abs(g)*A*(abs(g)'));   % Mode detection
                        B_modes(y_grid,x_grid,:) = diag(B2);        % Mode detection
                    end

                    g = sum(g,1);          % Sum all modes [207x64] -> [1x64]
                    psf(y_grid,x_grid) = abs(g*g_targ')^2 ; % For PSF
                    B(y_grid,x_grid,dm_freq,dm_zs) = g*(CSM.*A)*g'/(abs(g)*A*(abs(g)'));    % Beamforming

                end
            end
        end

        b_modes(1:total_modes,dm_freq) = abs(sum(sum(B_modes,1),2));
        Modes(1:total_modes,:,dm_freq) = [mode n_modes];

        psf = psf/max(max(psf));
        psf_w(dm_freq,dm_zs) = psf_w(dm_freq,dm_zs) + sum(sum(psf,1),2);
        PSF(:,:,dm_freq,dm_zs) = psf;
        time = toc;
        disp(['CSM freq layer: ' num2str(dm_freq) ', ' ...
            num2str(cont_freq) ' of ' num2str(length(layer)) ...
            ', frequency: ' num2str(f,3) 'Hz, ' ...
            ', z_s layer: ' num2str(dm_zs) ' of ' num2str(length(Z_S)) ...
            ', time spent: ' num2str(time,3) 's']);
        time_spent(dm_freq,dm_zs) = time;
        cont_freq = cont_freq + 1;
    end
end


%% output data

CBF_output = struct('CBFmap',B,...
    'PSF',PSF,...
    'x_mesh',x_mesh,...
```

```
    'PSFweight',psf_w,...
    'TimeSpent',time_spent,...
    'NumberOfModes',Number_of_modes,...
    'Modes',Modes,...
    'b_modes',b_modes,...
    'TotalModes',total_modes,...
    'MeshSize',N);

end
```